Journal of the Mechanics and Physics of Solids 59 (2011) 1623–1646

Contents lists available at ScienceDirect

Journal of the Mechanics and Physics of Solids

journal homepage: www.elsevier.com/locate/jmps

Failure mechanisms in composite panels subjected to underwater impulsive loads

Félix Latourte [a,1,2], David Grégoire [a,1,3], Dan Zenkert [b], Xiaoding Wei [a], Horacio D. Espinosa [a,*]

[a] Northwestern University, 2145 Sheridan Rd., Evanston, IL 60208-3111, USA
[b] KTH-Royal Institute of Technology, Sweden

ARTICLE INFO

Article history:
Received 28 August 2010
Received in revised form
19 March 2011
Accepted 15 April 2011
Available online 21 April 2011

Keywords:
Composite materials
Fluid–structure interaction
Dynamic failure
Delamination
Blast

ABSTRACT

This work examines the performance of composite panels when subjected to underwater impulsive loads. The scaled fluid–structure experimental methodology developed by Espinosa and co-workers was employed. Failure modes, damage mechanisms and their distributions were identified and quantified for composite monolithic and sandwich panels subjected to typical blast loadings. The temporal evolutions of panel deflection and center deflection histories were obtained from shadow Moiré fringes acquired in real time by means of high speed photography. A linear relationship of zero intercept between peak center deflections versus applied impulse per areal mass was obtained for composite monolithic panels. For composite sandwich panels, the relationship between maximum center deflection versus applied impulse per areal mass was found to be approximately bilinear but with a higher slope. Performance improvement of sandwich versus monolithic composite panels was, therefore, established specially at sufficiently high impulses per areal mass ($I_0/\bar{M} > 170\ \mathrm{m\,s^{-1}}$). Severe failure was observed in solid panels subjected to impulses per areal mass larger than $300\ \mathrm{m\,s^{-1}}$. Extensive fiber fracture occurred in the center of the panels, where cracks formed a cross pattern through the plate thickness and delamination was very extensive on the sample edges due to bending effects. Similar levels of damage were observed in sandwich panels but at much higher impulses per areal mass. The experimental work reported in this paper encompasses not only characterization of the dynamic performance of monolithic and sandwich panels but also post-mortem characterization by means of both non-destructive and microscopy techniques. The spatial distribution of delamination and matrix cracking were quantified, as a function of applied impulse, in both monolithic and sandwich panels. The extent of core crushing was also quantified in the case of sandwich panels. The quantified variables represent ideal metrics against which model predictive capabilities can be assessed.

1. Introduction

Glass reinforced plastic (GRP) composite materials are of current interest in naval hull construction (Mouritz et al., 2001), because they exhibit low weight and low magnetic signature. These are advantages of particular interest to naval

* Corresponding author.
E-mail address: espinosa@northwestern.edu (H.D. Espinosa).
[1] These authors contributed equally.
[2] Current affiliation: EDF–R&D, MMC, Avenue des Renardières, 77818 Moret-sur-Loing, France.
[3] Current affiliation: LFC-R, UMR5150, Université de Pau et des Pays de l'Adour, Allée du Parc Montaury, 64600 Anglet, France.

0022-5096/$ - see front matter © 2011 Elsevier Ltd. All rights reserved.
doi:10.1016/j.jmps.2011.04.013

designers interested in fast and stealth marine structures. Two different architectures are generally used to build composite hulls: single-skin design and sandwich construction, where a crushable core is encased between fiber-reinforced face skins. Both architectures involve the use of frames, stiffeners and bulkheads that provide the overall structural stiffness, and support the GRP monocoque or sandwich hull. In these constructions, the connection between the hull and the bulkhead does not seem to be a weak point when subjected to blast loading. Indeed, no localized shear or tearing was observed in full scale blast experiments (Hall, 1989). These experiments showed that deformation and damage are distributed on the sandwich panel itself, in which interlaminar delamination occurs. A visible change in opaqueness in the hull skin appeared after the impulsive loading (Hall, 1989).

Large scale field blast experiments have also been conducted. In these experiments, a 3D digital image correlation technique was employed to reconstruct the deformation histories of the tested panels (Dear et al., 2009). At the laboratory scale, experimental studies were conducted to study the dynamic response of composite sandwich beams subjected to projectile impact (Tagarielli et al., 2007; Johnson et al., 2009), the ballistic resistance of 2D and 3D woven sandwich composites (Grogan et al., 2007) and the impact response of sandwich panels (Schubel et al., 2005; Tekalur et al., 2008) with optimized nanophased cores (Bhuiyan et al., 2009; Hosur et al., 2008). The reader interested in the numerous experimental studies of marine composite subjected to impulsive loadings can refer to Porfiri and Gupta (2009). These studies present the performance of different composite panels and the most significant damage modes involved in blast or ballistic resistance of sandwich structures, whose local degradation can greatly affect the overall structural performance (Zenkert et al., 2005). One limitation of the experiments reported in the literature is that the impacted region is typically small compared to the panel or laminate dimension, resulting in very localized damage. Localized damage is also not representative of the structural effects observed in larger scale blast studies, where clamping tearing is not the most significant mechanism responsible for structural failure, and deformation and damage are spread over a large section of the hull.

Scaled down laboratory fluid–structure interaction experiments have been successfully developed and applied to the investigation of monolithic steel plates (Espinosa et al., 2006; Rajendran and Narashimhan, 2001) and sandwich steel constructions (Mori et al., 2007, 2009) by Espinosa and co-workers. In the present paper, the fluid–structure interaction (FSI) setup introduced in Espinosa et al. (2006) is utilized to characterize composite monolithic and sandwich plates. The advantage of this setup relies on the scaling of full field loads that enable the testing of panels with dimensions (radius $L=76.2$ mm) small enough to be easily manufactured and handled in a laboratory setting, but with sufficient thickness to investigate layups consistent with full marine hulls in terms of stacking sequence and number of plies. Moreover, the setup is highly instrumented and allows recording of deflection profile histories over the entire span of the panels for a precisely known applied impulse.

Composite panels subjected to blast typically present not only extensive interlaminar fracture (delamination) but also matrix microcracking and ultimately fiber fracture at the highest impulses. In sandwich panels, these failure modes are affected by interactions between the core and the facesheets. Therefore, substantial improvements in the panel performance rely on the core crushing behavior and the strength of the core-facesheet bond. As a general trend, soft cores are generally preferred since they can enhance energy absorption and blast mitigation, which is key in panel performance. Foam crushing is typically characterized by a stress plateau followed by densification and sudden increase in hardening. Among core materials, PVC foam and balsa wood cores were investigated because of their suitable crushing strength in naval applications. Unfortunately, very limited experimental data exists concerning the performance and failure of composite panels subjected to impulsive loading (Tagarielli et al., 2007; LeBlanc and Shukla, 2010). Therefore, understanding and quantifying failure modes in composite materials, as a function of applied impulse, is a topic of research that requires additional attention from the community.

Concerning the prediction of structural behavior and failure of monolithic and sandwich hulls subjected to impulsive loadings, limited work was reported in the literature (Deshpande and Fleck, 2005; Hoo Fatt and Palla, 2009; Tilbrook et al., 2009; Forghani and Vaziri, 2009). Although physically based, most models rely on homogeneous description of the composite material at the scale of the single ply or of the sub-laminate (Hashin, 1980; Hashin and Rotem, 1973; Puck and Schurmann, 1998). A research initiative called *world-wide failure exercise* attempted to rank and classify the numerous models available in the literature based on their performance to predict failure under various loading conditions (Hinton et al., 2002; Soden et al., 1998; Soden et al., 2002; Soden et al., 2004). Surprisingly, investigated models are unable to predict failure correctly over a wide range of quasi-static stress paths. Therefore, attempts to establish predictive capabilities for composite materials have to be considered with care. Detailed experimental validation needs first to be attempted, especially in dynamic situations for which the literature is scarce. In this context, recently introduced multiscale models (Ladeveze and Lubineau, 2002; Ladeveze et al., 2006; Espinosa et al., 2000; Latourte et al., 2009; Espinosa et al., 2009) accounting for microstructural damage mechanisms developed in the framework of Hashin's damage mechanics (Hashin, 1986) might be of significant benefit to the composite modeling community.

The objective of the present paper is to characterize composite panel performance in terms of impulse-deflection, using the experimental methodology introduced in Espinosa et al. (2006). Failure modes, damage mechanisms and their spatial distributions are identified and quantified for composite monolithic and sandwich panels subjected to underwater impulsive loading. The quantified variables represent ideal metrics against which model predictive capabilities can be assessed. The paper is structured as follows: first, the tested composite panels are described and details about the manufacturing are given. Then, the experimental results are presented. These latter sections recap briefly the

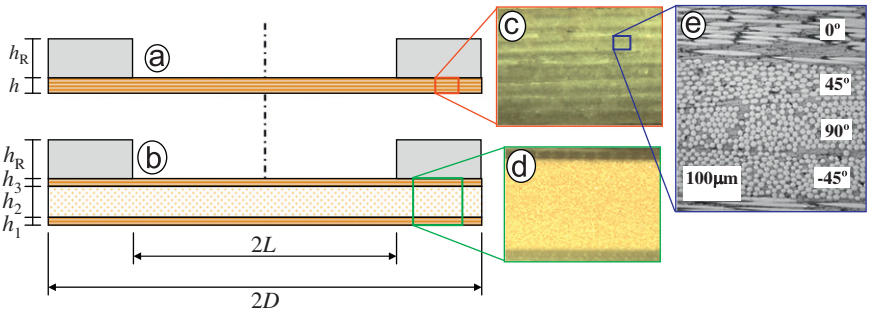

Fig. 1. Schematic of tested composite panels: (a) monolithic panel of thickness h bonded to a steel ring of thickness h_R, (b) sandwich panel with facesheet thicknesses h_1 and h_3 and core thickness h_2, (c) optical photograph of the solid panel cross section highlighting the different fabrics, (d) optical photograph of the sandwich panel cross section and (e) optical microscopy image of an E-glass/vinylester quasi-isotropic fabric used in the manufactured panels.

fluid–structure interaction experimental apparatus, and report impulse deflection performance and dynamic behavior of composite panels. A section is devoted to the study of damage modes identified post-mortem from an ultrasonic pulse-echo technique and optical microscopy. A summary of main findings and their implications is discussed in the closing section.

2. Description of composite panels

Composite solid, symmetrical sandwich and asymmetrical sandwich panels are considered in this study. The composite facesheets are comprised of quasi-isotropic Devold DBLT850-E10 glass-fiber (0/45/90/−45) non-crimp fabric infiltrated by vinylester Reichhold DION 9500 and the sandwich panels are built based on a 15 mm Diab H250 divinycell PVC foam core. Each composite fabric is composed of four laminas comprised of unidirectional E-glass fibers and assembled following the sequence: 0°/45°/90°/−45°. The fiber diameter, lamina and fabric thicknesses are 15, 150 and 600 μm, respectively. Fig. 1a and b describes the composite monolithic and sandwich panel geometries tested under the FSI experiment. Optical photography of the cross-sections are shown in Fig. 1c and d and an optical micrograph of an infiltrated fabric is shown in Fig. 1e.

Composite monolithic and sandwich panels of approximately the same weight per unit area were manufactured at KTH-Royal Institute of Technology, Sweden. After the manufacturing, the panels were cut with a water jet in order to obtain the final circular geometry (∅292.1 mm). Once the circular cut was performed, the panels were bonded to a steel ring of thickness h_R=25.4 mm (or h_R=19 mm for monolithic panels tested at low impulse) with a 3M Scotch-Weld™ DP460 epoxy adhesive. The three different specimen designs are

- Composite monolithic panels consisting of nine composite fabrics infiltrated by the resin: $(0/45/90/-45)_4$–$(45/90/-45/0)_5$. The final thickness obtained for solid panels was h=5.8 mm.
- Symmetrical sandwich panels consisting of six composite fabrics separated by a foam core: $(0/45/90/-45)_3$ - Core - $(45/90/-45/0)_3$. The final thickness obtained for symmetrical sandwiches was h=19 mm (h_1=2 mm, h_2=15 mm and h_3=2 mm).
- Asymmetrical sandwich panels consisting of six composite fabrics separated by a foam core: $(0/45/90/-45)_2$ – Core - $(45/90/-45/0)_4$. Final thickness obtained for asymmetrical panels was h=19 mm (h_1=1.33 mm, h_2=15 mm and h_3=2.66 mm).

The three designs listed above provide a similar areal mass to that of sandwich steel panels previously tested with the same fluid–structure interaction setup (Espinosa et al., 2006; Mori et al., 2007; Mori et al., 2009). The areal masses $\overline{M}$ of the monolithic, the symmetrical sandwich and the asymmetrical sandwich panels were 10.7, 11.3 and 11.2 kg m^{-2}, respectively. The principal mechanical properties of the constituents used in the manufactured panels are summarized in Table 1.

3. Fluid–structure interaction experiments

3.1. Experimental setup, performances and deformation histories

In order to reproduce in a laboratory setting underwater explosive loading conditions, a scaled fluid–structure interaction experimental setup was developed by Espinosa et al. (2006). During underwater blast loading, the impulsive load is characterized by an exponential decay pressure history depending on two parameters: the peak pressure p_0 and the time decay t_0 (Fig. 2). In the FSI experimental setup, the shell of a naval hull is scaled down to a composite panel specimen (Fig. 2). As described in Espinosa et al. (2006), the scaling is achieved by setting the same fluid–structure interaction as the one expected in the full scale application. In other words, the same fraction of the far field momentum, I_0, should be transmitted to the specimen. Defining the scaling factor, K, as the panel thickness in the full scale naval structure over the panel thickness in the experiment, i.e., $K=h_F/h_E$, the analysis shows that applied impulse should scale down by K (Espinosa et al., 2006).

Table 1
Constituent material properties.

	E-glass[a]	Resin[b]	Core[b]
Density (kg/m^3)	1850[c]		250
Tensile modulus (MPa)	73,000	3103	170
Tensile strength (MPa)	1900	70	8.7
Compressive modulus (MPa)	–	–	300
Compressive strength (MPa)	–	–	5.8
Shear modulus (MPa)	5500	1150	104
Shear strength (MPa)	–	42	4.5

[a] Properties estimated from experiments.
[b] Properties as certified by manufacturer.
[c] Mean density estimated on the actual panels after infiltration.

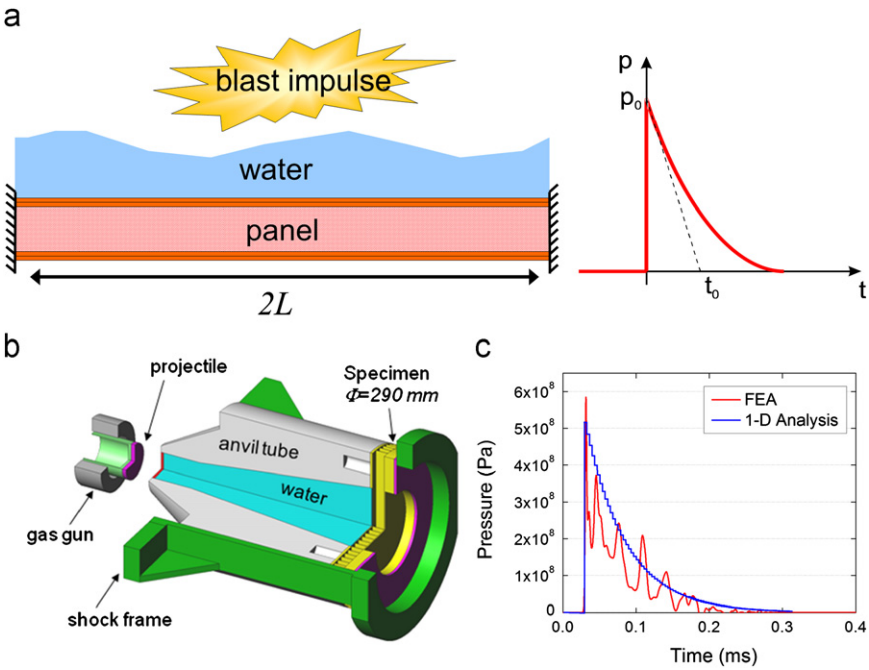

Fig. 2. (a) Schematics of underwater explosion conditions and pressure profile history; (b) schematic of blast simulator (Espinosa et al., 2006) and (c) example of pressure decay history as obtained from one-dimensional analysis (Espinosa et al., 2006) (blue curve) and FEA (red curve). (For interpretation of the references to color in this figure legend, the reader is referred to the web version of this article.)

As pressure does not scale down because it is an intensive quantity, impulse scaling is achieved by adjusting decay time t_0 through the dimensions of projectile and water piston. Another important consideration in the experimental design is the panel boundary condition. In the FSI setup, a steel ring is used to clamp the composite panels. The inertia of the steel ring simulates the structural bulkheads in a full scale naval structure. Moreover, this boundary condition allows for boundary core crashing in sandwich structures. A water piston seals the other extremity of the chamber and the exponentially decaying pressure history is produced by impacting the water piston with a flyer plate launched by a gas gun (Espinosa et al., 2006). After impact, pressure waves propagate through the water column and reach the composite panel. The circular part of the composite panel in contact with the water column is subjected to the impulsive load. When the panel deforms, water cavitation is elicited at the specimen–water interface. The deflection history of the loaded panel is characterized by means of shadow Moiré and high speed photography (Espinosa et al., 2006; Mori et al., 2007, 2009).

In previous experiments carried out on solid stainless steel panels (Espinosa et al., 2006), pressure histories recorded with pressure transducers were consistent with the predicted exponential decay associated with blast loading. The pressure wave created by the impact of the flyer plate on the water piston is a function of flyer initial velocity V_0, material impedance and flyer plate/water piston dimensions. As shown in Fig. 2c, the pressure decay history, at the anvil entrance, predicted by the one-dimensional analytical solution given in Espinosa et al. (2006), exhibits overall agreement with the pressure history obtained from a coupled Eulerian–Lagrangian finite element analysis (FEA) performed using ABAQUS/Explicit v6.9. However, we found from FEA simulations that at impact velocities in excess of 200 m/s, the generated impulse is also sensitive to other features, such as the geometry of the anvil tube, and dimensions and plastic flow of

projectile and water piston. Furthermore, impulse losses with propagation distance are also expected due to fluid viscosity. Therefore, here the free-field impulse near the panel is obtained from FEM simulations using an equation of state for water (Espinosa et al., 2006) and viscoplastic properties for the flyer and water piston. Contact between flyer and anvil, as well as between water piston and anvil, are also modeled with a friction coefficient of 0.1. Separate coupled Eulerian–Lagrangian simulations were performed on water columns extending beyond the location of the specimen. Hence, by specifying the experimental conditions, such as flyer plate velocity, anvil, flyer plate and water piston materials and geometries, the applied impulse for each experiment was obtained by numerically integrating the pressure history at the location of the tested panels. The decay time t_0 was obtained by dividing the impulse by the peak pressure.

In the work reported here, the panels are labeled by configuration and test number. Solid panel, symmetrical sandwich and asymmetrical sandwich configuration are respectively numbered as first, second and third. Hence, experiment 2-3 refers to the test #3 for the symmetrical sandwich configuration. In Table 2, panel configurations and corresponding impulse parameters are summarized. For all the experiments, except 2-4 and 3-2, the thickness of the water piston was 10.42 mm. Experiments 2-4 and 3-2 were conducted with flyer plates and water pistons of matching thicknesses. Impulses were varied from $I_0=1233$ Pa s (panel 1-1) to $I_0=6672$ Pa s (panel 3-2). Applied impulses per areal mass ($I_0/\overline{M}$) are also listed in Table 2 for each performed test. In order to examine the influence of the panel architecture on the deflection performance, panels with different construction types (monolithic and sandwich) were tested at comparable impulses. The last column of Table 2 provides the normalized peak deflection δ_{max}/L. For experiment 1-5, no peak deflection was obtained because the grating used in the shadow Moiré was damaged by flying debris. For experiment 1-4, the reported peak deflection was obtained prior to the panel massive delamination and failure as observed from high speed camera pictures and post-mortem imaging.

The performance of the composite panels in terms of normalized maximum deflection measured for an applied impulse per areal mass is shown in Fig. 3. Plotting on the same figure experimental results obtained on composite monolithic panels, composite sandwich panels and previous results obtained on A304SS sandwich panels with various core topologies (Mori et al., 2007; Mori et al., 2009), a comparison of performances is obtained. For sandwich panels, the maximum deflection on the airside is employed. This deflection is indeed a relevant performance indicator for blast protection in which personnel and equipment must be shielded. The experimental results for all tested panels are plotted in Fig. 3.

From the experimental results plotted in Fig. 3, the following observations can be drawn:

- The performance of composite solid panels follows a linear trend, as shown by the dashed line, leading to the following relation as determined from a least square linear fit:

$$I_0/\overline{M} = (935\ \delta_{max}/L - 13)(\mathrm{m\ s^{-1}}), \tag{1}$$

  where I_0 is the applied impulse X, $\overline{M}$ is the panel areal mass, δ_{max} is the peak deflection and L is half the panel span.
- The impulse deflection behavior of sandwich panels 2-1, 2-2, 2-3, 3-1 and 3-2 shows a bilinear relationship given by

$$\begin{aligned} I_0/\overline{M} &= (5561\ \delta_{max}/L - 884)(\mathrm{m\ s^{-1}}) \quad \text{for } I_0/\overline{M} < 430 \\ I_0/\overline{M} &= (4211\ \delta_{max}/L - 633)(\mathrm{m\ s^{-1}}) \quad \text{for } I_0/\overline{M} > 430. \end{aligned} \tag{2}$$

  Note the higher slope as compared to monolithic panels. The advantage of the sandwich architecture at high impulse per areal mass is therefore established.
- The effect of pressure history is illustrated by the performance of experiments 2-3 and 2-4. While both panels have been subjected to the same impulse but different peak pressure and decay time, their performance (see Fig. 3) and failure modes (see Section 3.3) exhibited quite distinct features.

Table 2
List of conducted experiments reporting impulse parameters and normalized peak deflections recorded during the experiments.

Geometry	Labels	Flyer plate thickness (mm)	Projectile velocity (m/s)	p_0 (MPa)	t_0 (μs)	Impulse I_0 (Pa s)	$I_0/\overline{M}$ (m s^{-1})	Normalized peak deflection δ_{max}/L
Solid panel	1-1	4.66	235	49.3	25	1233	116	0.151
	1-2	4.67	340	70.6	25	1766	166	0.188
	1-3	6.74	340	67.4	36	2425	227	0.257
	1-4	8.74	352	76.3	43	3283	314	0.350[a]
	1-5	10.82	368	76.3	57	4349	416	–
Symmetrical sandwich	2-1	6.74	343	68.5	36	2465	217	0.198
	2-2	10.67	339	72.4	55	3983	351	0.222
	2-3	13.42	360	101.5	55	5581	495	0.268
	2-4	16.38	308	62.4	87	5427	482	0.213[a]
Asymmetrical sandwich	3-1	10.87	333	68.1	58	3948	350	0.222
	3-2	16.59	367	75.8	88	6672	592	0.291

[a] Peak deflection preceding massive panel failure.

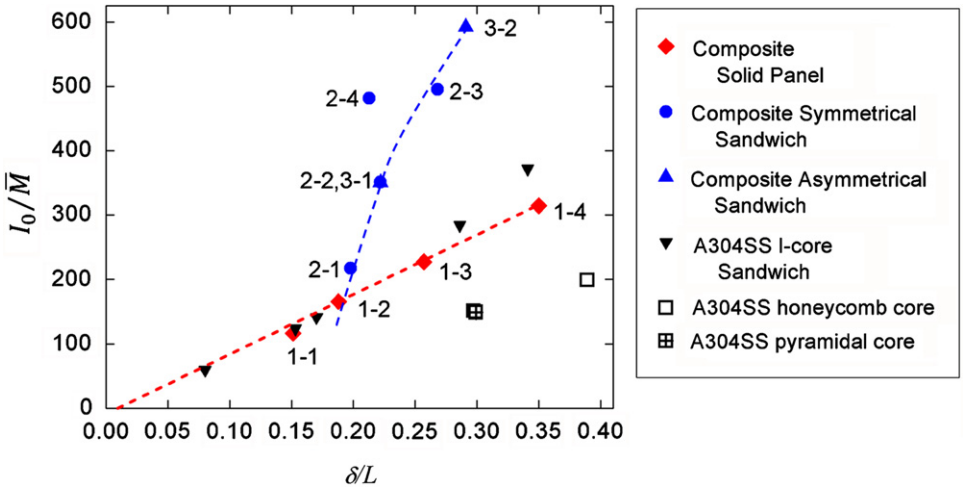

Fig. 3. Impulse per areal mass versus normalized deflection for monolithic and sandwich composite panels. The experimental results obtained on A304 stainless steel sandwich panels, reported in Mori et al, (2007, 2009), are overlaid for comparison.

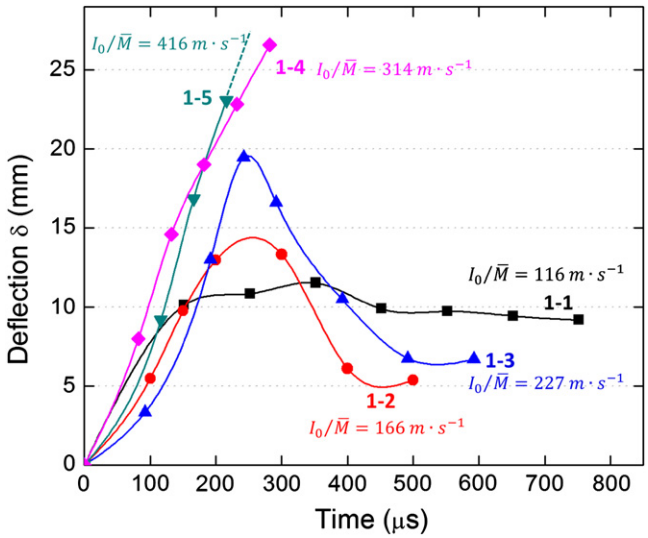

Fig. 4. Panel center deflection histories for monolithic panels (tests 1-1 to 1-5). During tests 1-4 and 1-5, panel failure prevented the observation of Moiré fringes after the last point plotted on the graph.

- The performance of composite monolithic panels in terms of impulse-deflection is comparable to the one observed for A304SS I-beam core steel sandwiches, which was identified as optimal core topology among all the different designs reported in Mori et al. (2007, 2009). By contrast, composite monolithic panels perform much better than A304SS panels with honeycomb or pyramidal cores. This highlights the performance-to-weight advantages of composite solid panels.
- Experiments 1-4, 2-3 and 3-2 exhibited extensive delamination and fiber failure with loss of impermeability as will be discussed later in Section 3.3.

3.1.1. Deformation histories in composite solid panels (tests 1-1 to 1-5)

Deflection profiles were calculated for all solid panels; typical results are presented in Appendix A. From the full profile sequence corresponding to each experiment, deflection at the panel center was extracted to plot deflection histories. In Fig. 4 the deflection history for all tested monolithic panels is given. In this figure, several features are noticeable:

- At the lowest impulse, experiment 1-1, $I_0/\overline{M}=116\ \mathrm{m\,s^{-1}}$, the peak deflection is reached slowly at $\sim$350 μs. A permanent deformation, recorded after the test, was less than 2 mm. Hence, the elastic recovery occurs at a very slow rate, and is not fully captured by the recorded images.

- At higher impulses (experiment 1-2 at $I_0/\overline{M}=166$ and experiment 1-3 at 227 m s^{-1}), the peak deflection δ_{max} is reached faster, at approximately 250 μs. An even faster rate of deformation is observed at higher impulses ($I_0/\overline{M}=314$ and 416 m s^{-1}).
- The spring back effect is more pronounced at $I_0/\overline{M}=166$ and 227 m s^{-1} than at $I_0/\overline{M}=116$ m s^{-1}. At $I_0/\overline{M}=227$ m s^{-1} the permanent deflection δ^{perm} was 5.2 mm, which is very close to the last value recorded using high speed photography in the frame at $t=592$ μs.
- For the two highest impulses $I_0/\overline{M}=314$ and 416 m s^{-1}, no spring back effect was measured because of the extreme nature of these experiments. As it will be shown later in the failure analysis section, extensive delamination and fiber failure occurred under these impulses, which prevented the recording of Moiré fringes beyond the initial increasing deformation phase.

3.1.2. *Deformation histories in composite sandwich panels (tests 2-1 to 2-4 and 3–1, 3–2)*

Composite sandwich panels were also subjected to underwater blast loading using the same methodology (cf. Table 2). Center deflection histories were computed and plotted in Fig. 5 for symmetric sandwich panels and in Fig. 6 for asymmetric sandwich panels. An additional result showing complete deflection profiles is presented in Appendix A.

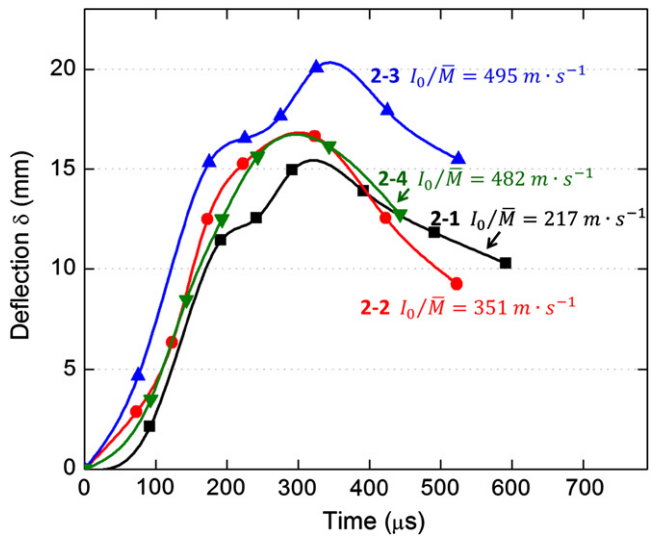

Fig. 5. Panel center deflection histories for composite symmetric sandwich panels.

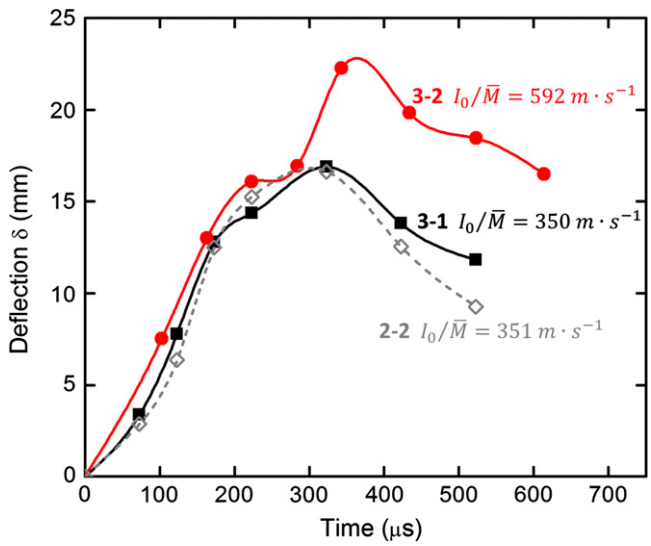

Fig. 6. Panel center deflection histories for composite asymmetric sandwich panels (exp. 3-1 and 3-2) at two different impulse levels. Center deflection history of experiment 2-2 (symmetric configuration) is also shown for comparison. Note that experiments 2-2 and 3-1 were performed at approximately the same impulse per areal mass.

Several features can be observed in Figs. 5 and 6:

- *Deflection profile shapes* in sandwich panels were similar over the range of applied impulses. Deflection profiles exhibit a symmetrical parabolic shape (Fig. 24). In the early increasing deflection stage ($t < 130$ μs), characteristics shoulders are observed on the center deflection histories.
- The *symmetrical* (test 2-2) and the *asymmetrical* (test 3-1) sandwich panels show a similar response up to peak deflection when subjected to comparable impulses per unit areal mass ($I_0/\overline{M}=351$and 350 m s^{-1}, respectively). The maximum deflections are almost identical and occur at approximately the same time. A difference in the rate of recovery is observed, with the asymmetric configuration exhibiting a slower rate, which can be associated to less damage in the airside facesheet.
- In all the sandwich panels, the peak deflection is reached in approximately 300–350 μs, while in most of the monolithic panels it was reached earlier in ~250 μs. This *delay to reach the peak deflection* can be explained by core compaction, which absorbs part of the impulsive load before it is transferred to the airside facesheet.
- During the initial increasing deformation phase, several distinct rates are observed. A first rapid increase in deflection, up to 200 μs, is observed in experiments 2-1, 2-3 and 3-2. Then, a slower rate of increase followed by another high rate up to peak deflection is observed. In the other experiments, 2-2, 2-4 and 3-1, the first initial increase in deflection is followed by a continuous and smooth reduction in the deflection rate leading to a peak deflection at approximately 350 μs. This difference in phase can be correlated to peak and decay time of the applied impulses (cf. Table 2). As such these features can be attributed to the FSI effect. In fact, in experiments 2-1, 2-3 and 3-2 peak stresses are high and decay times short when compared to experiments 2-2, 2-4 and 3-1.
- *At fixed applied impulse, peak pressure and decay time greatly affect the response of sandwich panels* as suggested by the deflection histories in sandwich panels 2-3 and 2-4 tested at $I_0/\overline{M}=495$and 481 m s^{-1}, respectively. Although the applied impulses are comparable, the decay time in the pressure history corresponding to test 2-4 was 58% longer than the one in experiment 2-3. This results in a peak deflection 26% larger in panel 2-3 than in panel 2-4. Moreover, failure mechanisms in these two panels were quite different (cf. Section 3.3).

3.1.3. Comparison in deformation histories between solid and sandwich panels

Fig. 7 compares center deflection profile histories for experiment 1-3 (solid panel) and experiment 2-1 (symmetrical sandwich panel) subjected to comparable impulses per areal mass, $I_0/\overline{M}=227$ and 217 m s^{-1}, respectively. The plot highlights the clear improvement in performance resulting from the sandwich construction. The deflection in the sandwich panel is reduced by 23% to the one in the solid panel, and correspondingly, the amount of damage in the back face sheet is highly reduced. The spring back rate is much slower in the sandwich case.

3.2. Non-destructive damage identification

A 3-D damage evaluation was performed on the tested panels by the pulse-echo technique, which has already been proven successful in the identification of damage of thick GRP laminates (Mouritz et al., 2000). In this study, ultrasonic

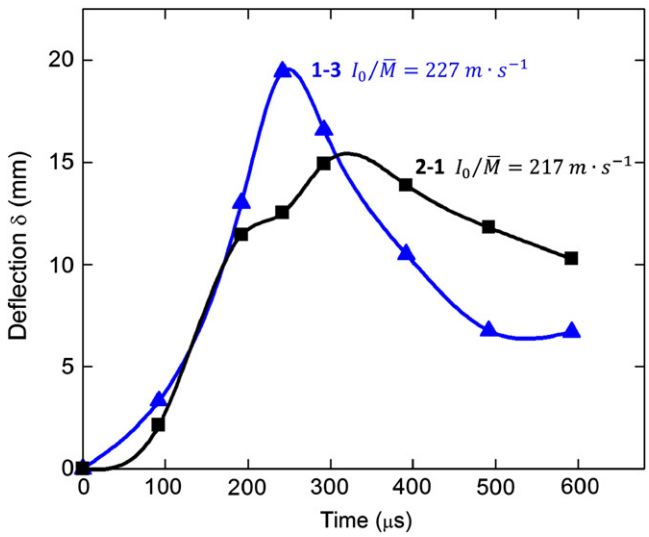

Fig. 7. Comparison between panel center deflection histories for solid (exp. 1-3) and symmetrical sandwich (exp. 2-1) panels at impulse per areal mass of $I_0/\overline{M}\sim220$ m s^{-1}.

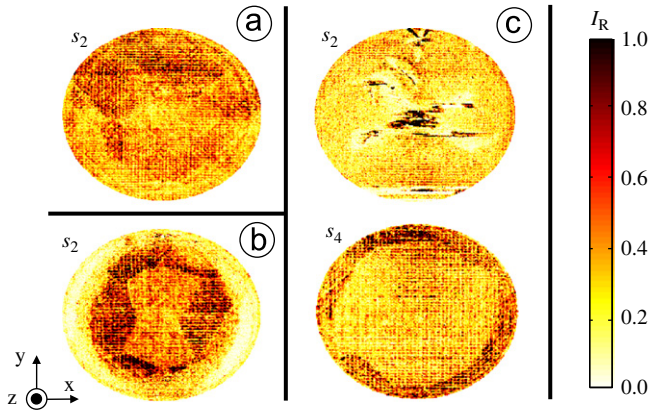

Fig. 8. C-scans obtained for solid panels 1-1 and 1-3 tested at impulses per areal mass of $I_0/\overline{M}=116$ m s^{-1} (a) and $I_0/\overline{M}=227$ m s^{-1} (b), respectively. C-scans obtained for the two facesheets of sandwich panel 2-3 tested at $I_0/\overline{M}=495$ m s^{-1}, (c) waterside facesheet (gate s_2) and airside facesheet (gate s_4). Gates are defined in Appendix B.

C-scans of the panels were performed by Sonoscan Inc., using a D9500™ C-SAM® apparatus. The scans were done in water-immersed conditions, with 10 MHz transducers. The scan speed was 380 mm/s and the monitored area was 182 by 182 mm covered by 768 by 768 pixels. This corresponds to a pixel size of 0.23 mm, which is sufficient to capture local variation within the panel section, of diameter $2L=152.4$ mm, subjected to the underwater blast loading. Details on the technique and employed data reduction procedures are discussed in Appendix B.

A summary of the main results obtained with the ultrasonic scanning technique are given in Fig. 8. At low impulse (subplot (a)), solid panels did not exhibit localized features associated with delamination, which was confirmed by optical microscopy on cross-sectional cuts (see below). At higher impulses per areal mass, $I_0/\overline{M}=$ 227 m s^{-1} (subplot (b)), a bright ring on the periphery was identified, which corresponds to bending induced delamination near the clamped boundary (the signal appears bright because of shadowing above the scanned region). Darker patches correspond to delamination within the mapped gate, while a brighter hourglass-shaped patch is noticed in the center of the panel where delamination is not present. Hence, the non-destructive evaluation (NDE) technique revealed delamination features, at sufficiently high impulse, that are more prominent on the periphery of the panels. The same type of delamination was found on the airside of sandwich panels subjected to $I_0/\overline{M}=495$ m s^{-1} (Fig. 8c), although its extent was much smaller. This is a remarkable sign of performance improvement resulting from the sandwich construction since delamination is reduced while the impulse per areal mass was doubled. At the same time, a cross shaped feature was revealed on the waterside, and correspond to visible cracks. We should note here that this type of crack is often not detrimental to the overall performance of the sandwich panels, as long as their integrity is preserved.

In the following section, we report post-mortem optical microscopy observations that will provide confirmation and further insight into the trends inferred from the pulse-echo scans.

3.3. Post-mortem microscopy

After having performed non-destructive evaluation with the pulse-echo technique, five panels (monolithic 1-1 and 1-3 and sandwich 2-3, 2-4 and 3-2) were sectioned along a diameter, oriented along the 0° or 90° axis, using a water jet machine. The two solid panels 1-1 and 1-3 were chosen to show the influence of the impulse magnitude, and because their dynamic deflection responses exhibited significant differences (see Fig. 4). The sandwich panels 2-3 and 2-4 were of interest because visible fiber failure was observed post-mortem but at different locations. The sandwich panel 3-2 was of interest because of its asymmetric configuration and because the panel was subjected to the highest tested impulse.

Photographs of the panel waterside taken before the cut are shown in Figs. 9a, 13a, 14a, 17a and 18a for experiments 1-3, 1-4, 2-3, 2-4 and 3-2, respectively. A dash line was superimposed to the cross section location where the cut was performed. Cross sectional views taken after the cut are shown in Figs. 17b, 13b, 14b, 17b and 18b. In some of these cross-sections, different areas, AM_i, where microscopy observations were conducted are shown. Photographs of the cross section of panel 1-1 are not reported but are similar in every aspect to the ones reported in Fig. 9 for panel 1-3.

A Nikon inverted DIC microscope Eclipse ME600 was used at 50 × magnification, fitted with a ProgRes Capture Pro 2.5 cooled CCD camera, to acquire sequence of images on the surface of the different panel cross-sections. These sequences covered the areas AM_i, and are shown in Figs. 10, 12, 15 and 16. Each individual picture has a resolution of 1360 by 1024 pixels, with a pixel size of 2.55 μm. Higher magnification pictures were also acquired to image matrix microcracking.

Two failure mechanisms were identified and analyzed based on the cross-sectional microscopy study. We will start by discussing trends in delamination for monolithic and sandwich panels subjected to increasing impulses. Second, an analysis of matrix microcracking distributions will be conducted for two solid panels, experiments 1-1 and 1-3.

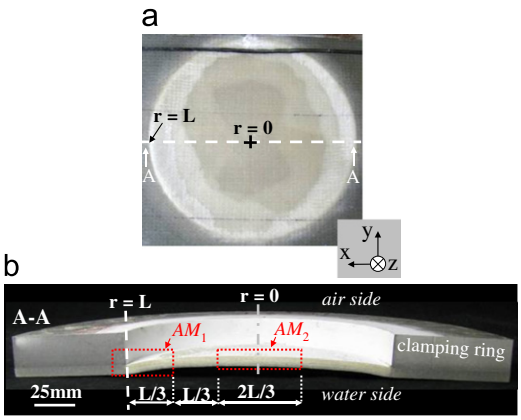

Fig. 9. Optical photography of solid panel tested at $I_0/\overline{M}=227$ m s^{-1} (exp. 1-3). (a) impacted side (waterside) of the panel showing whitened areas within the region subjected to water pressure. The line A–A corresponds to the cross-sectional cut. (b) Panel cross section A–A showing the steel ring bonded to the composite panel. A permanent deflection is observed, with a center residual deflection of 5.35 mm. The regions AM_1 and AM_2 correspond to the micrographs reported in Figs. 10a and 20a, respectively.

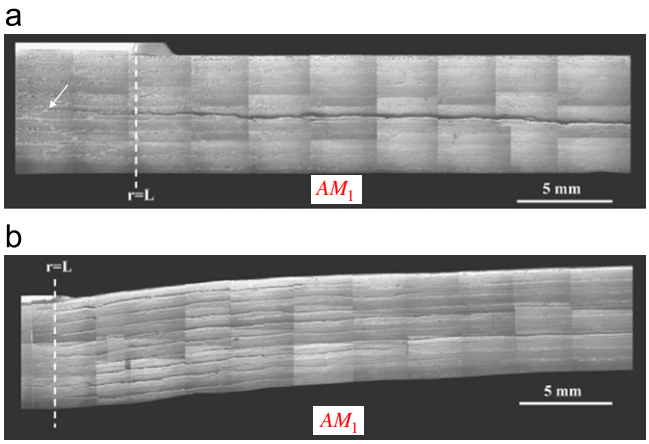

Fig. 10. Optical microscopy pictures in the clamped region AM_1 of solid panels 1-1 (a) and 1-3 (b), tested at $I_0/\overline{M}=116$ and 227 m s^{-1}, respectively. Delaminated interfaces are clearly observed, which typically propagate somewhat in the clamped region. In the case of panel 1-1, the tip of the delaminated interface is indicated by an arrow.

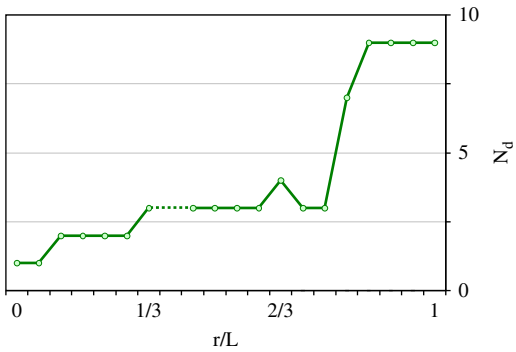

Fig. 11. The number of delaminated interfaces N_d in the monolithic panel 1-3 tested at $I_0/\overline{M}=227$ m s^{-1} (experiment 1-3) versus normalized radial position r/L.

3.3.1. Cross-sectional microscopy: monolithic panels

The clamping regions of monolithic panels 1-1 and 1-3 are shown in Fig. 10a and b, respectively. These regions cover around one quarter of the panel radius, L. The edge of the clamping ring, located at $r=L$, corresponds to the white dashed line. Tested at an impulse of $I_0/\overline{M}=116$ m s^{-1}, panel 1-1 exhibits a single delamination plane located at the panel half thickness. The delamination propagated within the clamped region of the sample, over a distance of approximately 5 mm.

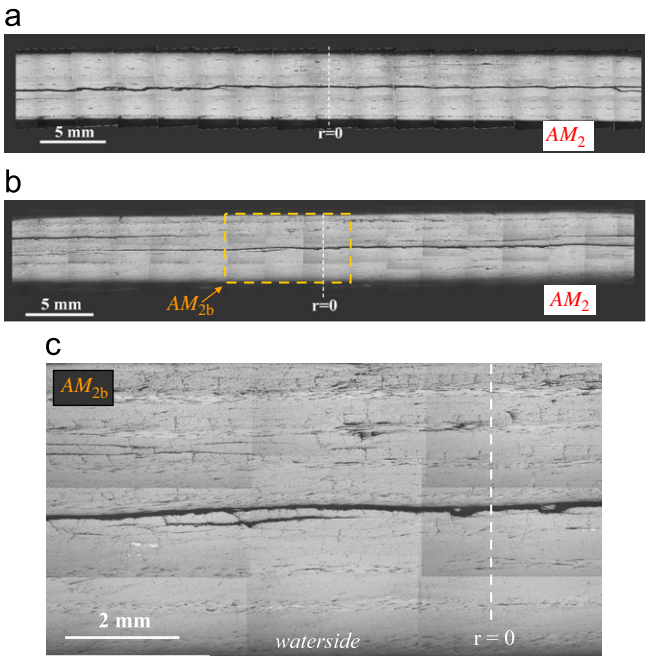

Fig. 12. Optical microscopy pictures in the center region AM_2 of solid panels 1-1 (a) and 1-3 (b), tested at $I_0/\overline{M}=116$ and 227 m s^{-1}, respectively. These sets of micrographs highlight the presence of delamination mostly located in the middle plane of the panel in both cases. (c) Magnified view of the central region AM_{2b} of panel 1-3 showing matrix cracking patterns in several fabrics.

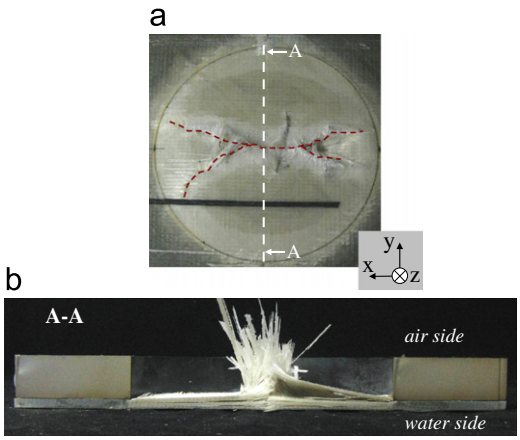

Fig. 13. Post-mortem photography of monolithic panel 1-4 tested at $I_0/\overline{M}=314$ m s^{-1}: (a) waterside facesheet photography showing the location of the cross section A-A and (b) cross sectional view highlighting massive fiber failure and delamination.

The delamination path is not constrained to a unique interlaminate interface but it rather jumps across interfaces within the laminate. A much larger number of delaminated interfaces, N_d, is found in panel 1-3 tested at a higher impulse of $I_0/\overline{M}=227$ m s^{-1}. At the clamping edge, $r=L$, eight delaminated interfaces are present but the delamination intensity and N_d decrease as the radial coordinate r decreases. The number $N_d=8$ corresponds to the number of interfabric interfaces, since nine fabrics were used in the panel construction. Once again, the delaminated interfaces are not strictly following the interfabric interfaces but more generally following interply interfaces, crossing plies freely all over the monitored cross section.

In the central regions of the two solid panels, less noticeable differences are observed in delamination trends (see Fig. 12a and b). In panel 1-1, a straight delaminated plane at half thickness is clearly observed over the whole area AM_2 (Fig. 12a). In panel 1–3, multiple delaminated planes coexist but are also located mostly at half thickness and in the upper region of the cross section. Unlike the delamination pattern observed in the clamping region, at $r=0$, $N_d=1$ in both cases.

The delamination observed in the solid panels is consistent with bending and stretching states (Jones, 1989). Bending of circular plates is maximal in the clamping region, inducing shear deformations, while equi-biaxial stretching is prominent in the plate center. In panel 1-3, the higher delamination observed at the clamping region decreasing progressively toward

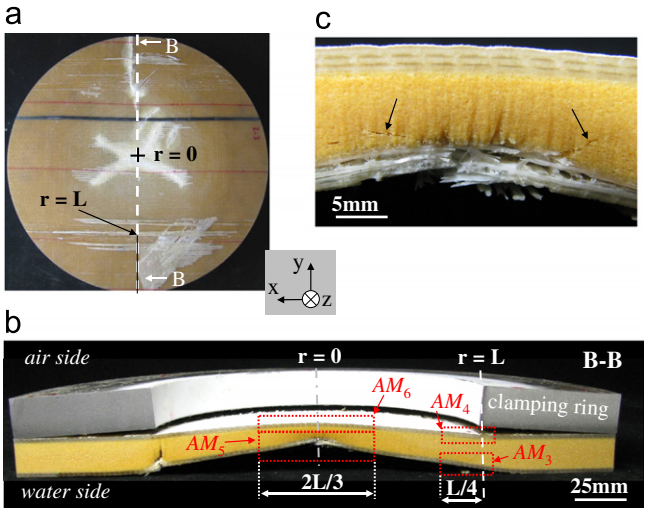

Fig. 14. Optical photography of sandwich panel 2-3 tested at the impulse of $I_0/\overline{M}$=495 m s^{-1}, after the experiment. (a) Impacted side (waterside) of the panel showing cross-shaped fracture within the central region, together with a few debonded fibers in the clamped area. The profile B-B corresponds to the cross-sectional cut. (b) Panel cross section B-B showing the plastically deformed steel ring debonded from the composite panel. Permanent center deflections are observed (5.65 mm for the airside facesheet and 14.2 mm for the waterside facesheet). The areas AM_i correspond to the micrographs reported in Figs. 15 and 16. (c) Magnified view of the cross section B-B taken in the panel center section. Arrows highlight the presence of slanted cracks in the foam.

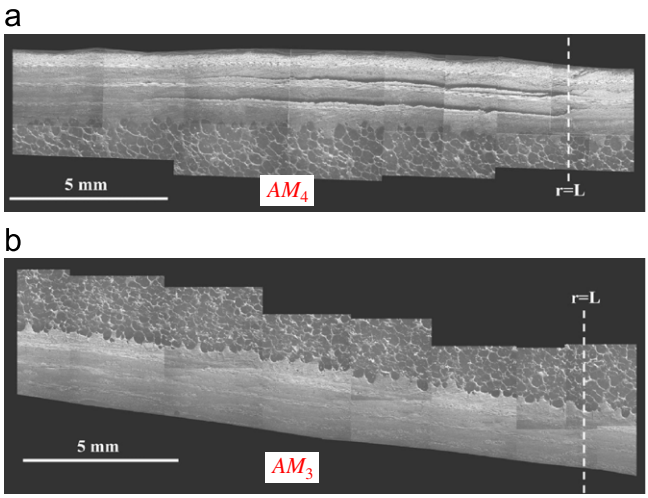

Fig. 15. Optical microscopy pictures for sandwich panel 2-3, tested at $I_0/\overline{M}$=495 m s^{-1}, in the airside clamped region AM_4 (a) and waterside clamped region AM_3 (b). The airside clamped region shows delamination patterns, while no delamination can be observed on the waterside.

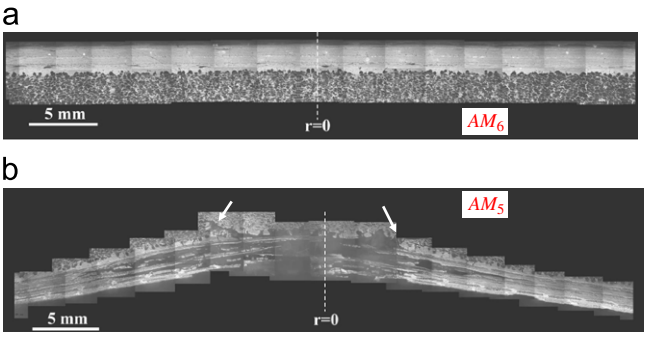

Fig. 16. Optical microscopy pictures for sandwich panel 2-3, tested at $I_0/\overline{M}$=495 m s^{-1}, in the airside central region AM_6 (a) and waterside central region AM_5 (b). The airside clamped region seems intact, while massive delamination and fiber failure can be observed on the waterside facesheet.

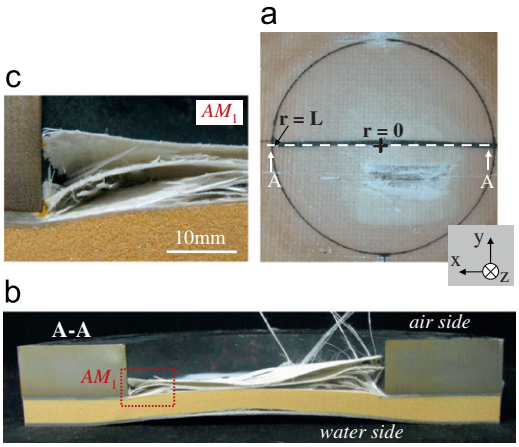

Fig. 17. Post-mortem images of symmetric sandwich panel tested at $I_0/\overline{M}=482$ m s^{-1} (exp. 2-4): (a) intact waterside facesheet image and location of the cross section A-A, (b) cross sectional view highlighting severe delamination and boundary fracture in the airside facesheet and (c) magnified view of area AM_1 at the vicinity of the steel ring.

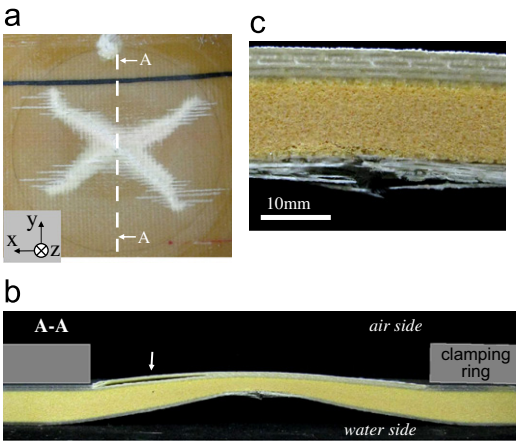

Fig. 18. Post-mortem images of asymmetric sandwich panel tested at $I_0/\overline{M}=592$ m s^{-1} (exp. 3-2): (a) waterside facesheet image showing cross pattern and location of the cross section A-A; (b) cross sectional view revealing extensive delamination in the airside (see white arrow) and core crushing; and (c) magnified view of the cross section in the panel center showing delamination and fiber fracture in the water facesheet.

the center is a direct consequence of the bending mode, which develops at the early stages of deformation (see Fig. 23). For this panel, the evolution of the number of delaminated interfaces N_d, as a function of normalized position, is shown in Fig. 11.

It is worth noting that observations from NDE are consistent with delamination observed by post-mortem microscopy. Indeed, delamination flaws are the only detectable defects from the NDE signatures. Matrix cracking was not captured due to their size and orientation. Both, NDE and microscopy techniques reveal that delamination is more significant in the boundary than in the center of the panel beyond a threshold applied impulse.

In the case of the monolithic panel tested at $I_0/\overline{M}=314$ m s^{-1} (exp. 1-4), a cross-shaped damage region extending the full length, $2L$, is observed in Fig. 13a. The cross sectional view of the panel shows that this macroscopic manifestation of failure is associated with severe delamination and massive fiber fracture along the path of the macroscopic cracks.

3.3.2. Cross-sectional microscopy: sandwich panels

Optical microscopy was also performed for several of the tested sandwich panels. Fig. 14 shows optical images of sandwich panel 2-3 tested at $I_0/\overline{M}=495$ m s^{-1}. An image of the waterside facesheet is shown in Fig. 14a. A cross-shaped fracture pattern is observed in the central region of the panel. The residual deformed shape and extend of core compaction are shown in Fig. 14b. Details of the waterside facesheet fiber fracture and delamination, as well as cracks in the PVC core, are shown in Fig. 14c.

Microscopy images of the clamped region are shown in Fig. 15a and b and images of the central region are shown in Fig. 16a and b. Similarly to solid panels, a bending induced delamination can be observed in the airside facesheet of the sandwich panel, in contact with the clamping ring. However, the delamination extent of approximately 13.5 mm is small when compared to the one observed in solid panels subjected to similar levels of impulse (Fig. 10b). A ring that

corresponds to the delaminated interfaces observed by microscopy was also revealed by NDE in the airside facesheet of panel 2-3 (see maps s_4 and s_6 in Fig. 29).

No delamination is observed near the support on the waterside facesheet, Fig. 16b. Interestingly, edge bending effects are limited on the waterside, as a result of extensive foam crushing. Similar behavior was observed in soft core steel sandwich panels tested with the same experimental apparatus (Mori et al., 2009).

In all solid and sandwich panels, the presence of delamination corresponds to bending effects with transverse waves traveling from the support to the panel center. This bending effect was also revealed by real time measurement during the experiment, and is provided by classical closed form solution of panels, clamped at the edges, and subjected to impulsive loads (Jones, 1989). Comparison of Figs. 10 and 15 shows that the delamination extent is significantly reduced in sandwich panels when compared to solid panels.

In the central region of the sandwich panel, massive failure (delamination, matrix cracking and fiber fracture) is observed on the waterside facesheet, see Figs. 14c and 16b. In addition to extensive damage in the waterside facesheet, two slanted cracks propagated in the core over a few millimeters (see arrows in Fig. 14c). Despite the extensive damage exhibited by the waterside facesheet, in the central region, no significant cracking or delamination could be found on the airside facesheet (Fig. 16a).

The effect of decay time on failure modes can be assessed when comparing experiments 2-3 ($I_0/\overline{M}=495$ m s^{-1}, $p_0=101.5$ MPa, $t_0=55$ μs) and 2-4 ($I_0/\overline{M}=482$ m s^{-1}, $p_0=62.4$ MPa, $t_0=87$ μs). As highlighted in the discussion of Fig. 14, in experiment 2-3 the composite panel exhibits a cross shape macroscopic crack on its waterside facesheet, while the airside facesheet remains intact. By contrast, in sandwich panel 2-4, no appreciable fiber failure is observed on the waterside facesheet of the specimen, Fig. 17a. Likewise, no significant core crushing in the central region, typical of strong cavitation associated to fluid–structure interaction, is observed. On the airside, the facesheet exhibits a high degree of delamination and fiber failure along the periphery, where the steel ring provides inertial support.

The effect of a non-symmetric weight distribution in sandwich construction was assessed through comparison of experiments 2-4 ($I_0/\overline{M}=482$ m s^{-1}, $p_0=62.4$ MPa, $t_0=87$ μs) and 3-2 ($I_0/\overline{M}=592$ m s^{-1}, $p_0=75.8$ MPa, $t_0=88$ μs). These two experiments were both conducted with long pressure decay time but the asymmetric panel was subjected to a higher impulse. As seen in Fig. 18, a cross-shaped fracture pattern was induced on the waterside facesheet. Delamination on the airside facesheet of the asymmetric panel is noticed but much reduced when compared to the symmetric panel (experiment 2-4). However, extensive foam crashing and fiber fracture on part of the boundary of the airside facesheet and in the center of the water facesheet are observed (Fig. 17b and c).

3.3.3. Quantification of stress-induced matrix cracking

Matrix damage in composites materials results from fiber/matrix interactions and can precede delamination (Marshall et al., 1985). Matrix damage and delamination are the two most significant damage mechanisms in composite materials; therefore their spatial characterization is essential in understanding the performance degradation of impacted structures. At high stresses, when matrix strength is exhausted and delamination has occurred, fibers can fail leading to ultimate failure of the structure. Hence, assessing matrix damage and particularly its distribution is an essential part of the damage identification. It also provides useful information about the structural state of the panel after having been subjected to impulsive loading. Macroscopically, matrix cracking results in a loss of structural stiffness since local load bearing capacity is reduced. A literature review of research conducted to build relationships between matrix cracking and stiffness loss was reported in (Lim and Hong, 1989), which presents several finite fracture mechanics approaches encompassing shear lag models (Lim and Hong, 1989) and the variational approach proposed by Hashin (1985, 1986).

All these analyses were developed in the framework of symmetrical cross-ply laminates loaded in tension in which cracks appear in the transverse layer. Hashin's method provided an accurate prediction of the stiffness loss of tensile samples that were successfully compared to experiments conducted on samples of different materials. It also provides a local estimation of stresses, and predicts the degradation of the transverse modulus and the shear modulus. Therefore, in this work we will employ Hashin's model. The reader interested in the formulation of the model can refer to Hashin (1985). In short the energy attributed to the crack perturbation is formulated for compatible stresses, and the complementary energy theorem is applied to find stress intensity factors and residual stiffness coefficients for a given intercrack distance.

Evolution of matrix cracking in laminated composite typically stops when the *Characteristic Damage State* (CDS) is attained. Observed experimentally (Abrate, 1991), such state corresponds to a saturation in crack density (minimal distance between cracks) and total stiffness reduction of a laminate cracked layer. Hashin's model is able to capture this asymptotic behavior with high precision due to the formulation of close crack interaction.

From high magnification images, acquired using optical microscopy, it was possible to measure the crack spacing as a function of radial position and ply in the cross-section of specimens 1-1 and 1-3. The crack distribution was identified separately on each lamina with fibers crossing the observation plane aligned with the 0° orientation of the layup. For this reason, cracks were only counted in plies of orientation 45°, 90° and −45° (3 every 4 plies). Intervals of 4 mm were defined and a crack density c (number of cracks per mm in the direction transverse to the fibers) was obtained for each measured lamina and each interval covering the radius. Cracks were only counted when showing a sufficient contrast on the picture and crossing the lamina entire thickness. To relate the measured crack density, c, and crack distance $2a$, to the damage variable, d, we use Hashin's formulas for axial stiffness degradation.

According to the variational approach introduced by Hashin (1985), the longitudinal stiffness $E_x(c)$ of a cross-ply 0°/90°/0° laminate can be computed from the undamaged (initial) stiffness E_x^0, the axial and transverse moduli E_A and E_T, the axial and transverse Poisson ratio ν_A and ν_T, and the axial and transverse ply thicknesses t_1 and t_2 according to the following set of equations:

$$\frac{1}{E_x} \leq \frac{1}{E_x{}^0} + \frac{4}{E^T} k_1^2 \eta(\lambda)\alpha(\alpha^2+\beta^2)t_1 c, \quad \text{when } (a/t_1) \gg 1, \tag{3}$$

$$\frac{1}{E_x^*} \leq \frac{1}{E_x^0} + \frac{k_1^2}{\lambda+1}\left(\frac{1}{E_T}+\frac{1}{\lambda E_A}\right), \quad \text{when } (a/t_1) \to 0, \tag{4}$$

with

$$\begin{aligned}
&k_1{}^{-1} = \left(\tfrac{t_1}{h} + \tfrac{E_T}{E_A}\tfrac{t_2}{h}\right) && p = (C_{02}-C_{11})/C_{22} \\
&\eta(\lambda) = (3\lambda^2+12\lambda+8)/60 && q = C_{00}/C_{22} \\
&\lambda = (t_2/t_1),\ h = t_1+t_2 && C_{00} = 1/E_T + 1/\lambda\, E_A \\
&\alpha = p^{1/4}\cos(\theta/2) && C_{02} = (\nu_T/E_T)(\lambda+2/3) - (\nu_A\lambda/3E_A) \\
&\beta = q^{1/4}\sin(\theta/2) && C_{22} = (\lambda+1)(3\lambda^2+12\lambda+8)/60E_T \\
&\theta = \tan^{-1}\left(\sqrt{(4q/p^2)-1}\right) && C_{11} = \tfrac{1}{3}(1/G_T + \lambda/G_A)
\end{aligned} \tag{5}$$

The stiffness reduction given by Eqs. (3) and (4) is valid for cross-ply laminates. While Eq. (3) gives the lower bound of the degraded stiffness for far apart cracks, Eq. (4) provides the expression of degraded stiffness E_x^* associated to the Characteristic Damage State (CDS) when the smallest intercrack distance is observed and the stiffness loss in the cracked layer is maximal ($d=1$). One difficulty of quantifying damage in the material tested in this work is the absence of analytical solutions from matrix cracking in non-orthogonal laminates, which lack symmetry. However, finite element simulations have been compared to experiments on quasi-isotropic laminates (Singh and Talreja, 2009), and comparable matrix cracking mechanisms to those in orthogonal laminates were predicted. For this reason, the Hashin model for orthogonal laminates is assumed to provide a reasonable estimation of damage induced by matrix cracking in a quasi-isotropic laminate. Relationships between matrix damage d and crack density c in each ply of the quasi-isotropic fabric used in the composite panels studied in this work could then be obtained.

In the specimens investigated here, the thicknesses t_1 and t_2 of the axial and transverse plies were chosen to be 0.225 and 0.075, respectively, based on a laminate thickness h of 0.6 mm, corresponding to the fabric thickness, and a ply thickness of one quarter the fabric thickness. Eqs. (3) and (4) were then employed using the lamina elastic constants E_T, E_A, ν_T, ν_A, G_T and G_A listed in Table 3. These material coefficients were obtained from Daniel et al. (2006). $E_x^0 = 15.7$ GPa is obtained experimentally for our quasi-isotropic layup. In the following, Eqs. (3) and (4) are considered to be true at the limit, providing thus a lower bound estimation of degraded stiffness. The local matrix tensile damage variable d of the cracked ply is finally obtained by interpreting the stiffness reduction of the cross-ply lamina using the relationship:

$$d(c) = \min\left(\left(1-\frac{E_x-E_x^*}{E_x^0-E_x^*}\right), 1\right). \tag{6}$$

Note that the damage variable is bounded by $d(c)=0$ at the initial state ($E_x = E_x^0$) and $d(c)=1$ when $E_x \leq E_x^*$ (complete stiffness loss of the cracked layer).

The matrix damage d as a function of radius r, for specimen 1-3, is given in Fig. 19. In this plot, 8 sets of points and curves are shown corresponding to the fabrics f_i that were measured using microscopy. Among the 9 fabrics of the monolithic fabric, f_1 corresponds to the waterside while f_9 corresponds to the airside of the panel. Each point corresponds to an averaged d computed in each 4 mm long interval within a given fabric. Some scattering is observed in the data, which could be attributed to measurement noise and low typical number of cracks per ply in each measured interval (~2–6 in average). Smoothing splines are plotted together with the experimentally sampled data to better represent variations in mean damage values. Such variations are noticeable: higher d values close to 1 (complete loss of stiffness) are observed in the central part of the specimen for $0 < r/L < 1/3$, while damage progressively diminishes towards the supported boundary. A high damage is also seen in the vicinity of the supporting ring ($r/L=1$), which indicates some effect of local shear and

Table 3
Lamina elastic constants for E-glass/vinylester.

Coefficient	Axial stiffness E_A (GPa)	Poisson ratio ν_A	Shear modulus GA (GPa)
Value	39	0.28	3.5
Coefficient	Transverse stiffness E_T (GPa)	Poisson ratio ν_T	Shear modulus G_T (GPa)
Value	12	$(E_T/E_A)\nu_A = 0.0862$	3

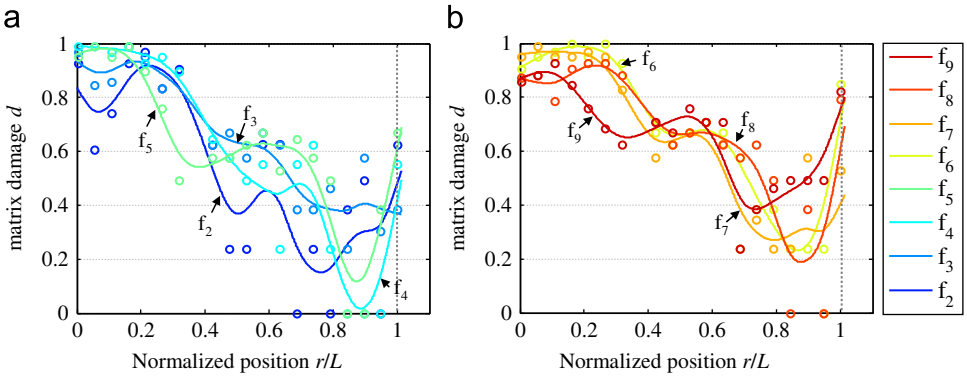

Fig. 19. Distribution of matrix damage in each analyzed fabric f_i in the composite monolithic panel tested at $I_0/\overline{M}=227$ m s^{-1} (exp. 1-3) as a function of the normalized radial position r/L: (a) waterside fabrics and (b) airside fabrics.

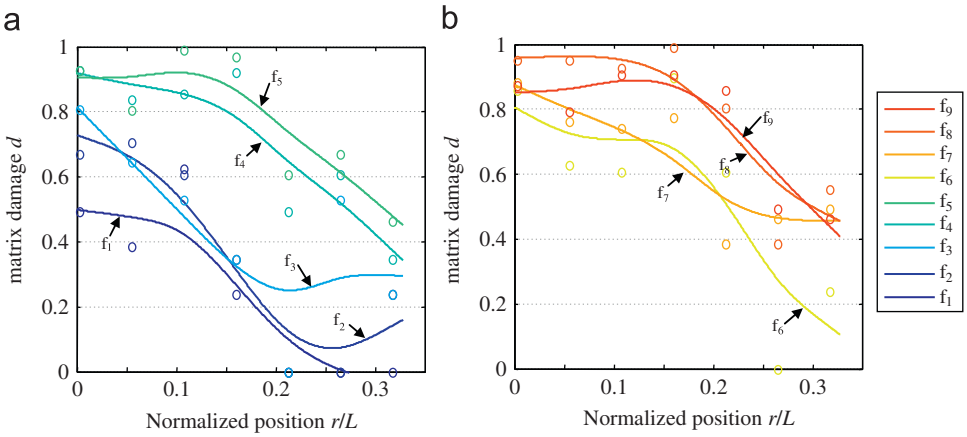

Fig. 20. Distribution of matrix damage, as a function of the normalized radial position r/L, in each analyzed fabric f_i of the composite monolithic panel tested at $I_0/\overline{M}=116$ m s^{-1} (exp. 1-1): (a) waterside fabrics and (b) airside fabrics.

stress concentrations induced by the support. It is interesting to notice that delamination (see Fig. 11) and matrix damage vary in opposite directions along the radius of panel 1-3:

- the matrix damage $d(c)$ is the highest in the center where biaxial stretching is maximal and decreases towards the boundary of the panel,
- A higher number of delaminated interfaces N_d are observed near the boundary, where bending-induced transverse loading is maximal, with a continuous reduction towards the panel center.

The damage distribution was also computed in the central section of the monolithic panel 1-1 tested at$I_0/\overline{M}=116$ m s^{-1} (see Fig. 20). A significant reduction in matrix damage, d, as the normalized position r/L increases can be observed. Differences between airside and waterside fabrics appear: more damage is observed in the airside fabrics (f_6–f_9) than in the waterside fabrics (f_1–f_5), which is consistent with the fact that stretching is higher on the airside because of the structural response of the panel. By contrast, less variations in damage were observed in experiment 1–3 ($I_0/\overline{M}=227$ m s^{-1}), where damage values were higher in the central section and very close to 1.

4. Discussion and concluding remarks

An assessment of the performance of composite monolithic and sandwich panels was presented in this article. Using a fluid–structure interaction experimental apparatus, the deflection profile histories of composite panel specimens were recorded by shadow Moiré and high speed photography. The performance of each panel was identified by plotting the peak center deflection versus applied impulse per areal mass. A linear relationship between center peak deflection versus applied impulse per areal mass was obtained for composite monolithic panels, similar to the behavior experimentally observed for steel monolithic panels (Rajendran and Narashimhan, 2001; Xue and Hutchinson, 2003; Nurick and Martin, 1989; Nurick and Shave, 1996; Teeling-Smith and Nurick, 1991; Rajendran and Narasimhan, 2006). For composite sandwich panels, the relationship between center peak deflection versus applied impulse per areal mass is also linear but

with a higher slope and negative intercept (see Fig. 3). Performance improvement of sandwich versus solid composite panels was, therefore, established specially at sufficiently high impulses per areal mass ($I_0/\overline{M} > 200$ m s^{-1}).

The performance of composite monolithic panels in terms of impulse-deflection was similar to the one observed for A304SS I-beam core steel sandwiches, which was identified as an optimal core topology among all the investigated designs (Mori et al., 2007, 2009; Hutchinson and Xue, 2005; Dharmasena et al., 2010; Liang et al., 2007). By contrast, composite monolithic panels perform better than A304SS panels with honeycomb or pyramidal cores. This highlights the properties to weight advantages of composite solid panels. Because of the low weight of glass-polymer composites, higher thicknesses h are obtained at fixed areal mass, which results in a higher bending stiffness.

The study also shows that different through thickness weight distributions, asymmetric versus symmetric, do not result in significant performance improvements. In this investigation, symmetrical (test 2-2) and asymmetrical (test 3-1) sandwich panels showed a similar response when subjected to comparable impulses per areal mass, 351 and 350 m s^{-1}, respectively. This is in part because even when a thinner front sheet results in overall less transmitted momentum (Vaziri et al., 2007; Xue and Hutchinson, 2004), enhanced fluid–structure interaction effect, the kinetic energy that has to be absorbed by the structure is higher.

Severe failure was observed in solid panels subjected to impulses per areal mass $I_0/\overline{M} > 310$ m s^{-1}. Extensive fiber fracture occurred in the center of the panels, where cracks formed a cross pattern through the plate thickness, and delamination was very extensive on the sample edges due to bending effects. Similar levels of damage were observed in sandwich panels but at a much higher impulse per areal mass. The effect of pressure history was illustrated by the performance characterized through experiments 2-3 and 2-4. While both panels were subjected to approximately the same impulse per areal mass, although with different peak pressure and decay time, their performance and failure modes exhibited distinct features. For the shorter decay time and higher peak pressure, a higher peak deflection was observed and failure occurred in the waterside facesheet. For the longer decay time and lower peak pressure, failure was due to shear tearing near the boundary resulting in delamination and fiber failure on the airside facesheet. The failure mechanisms, damage types and deflection trends are summarized in Table 4. The table highlights a few correlations, e.g., the correlation between fiber damage and development of visible cracks. In the case of solid panels, conical deflection profiles correlate with panel massive failure including formation of cracks, while more parabolic shapes were not associated to such failure.

The experimental work reported in this paper encompasses not only characterization of the dynamic performance of monolithic and sandwich panels, but also post-mortem characterization by means of both non-destructive and destructive techniques. Firstly, a non-destructive evaluation (NDE) was conducted by means of a C-scan pulse-echo technique. Then, optical microscopy was conducted on samples obtained by cutting the panels along their diameter. The NDE pulse-echo technique was employed to identify the presence of delamination on the entire panel. From the pulse-echo technique, qualitative information was obtained on the distribution of flaws in the panels. In solid panels, flaws appeared with more clarity at higher impulses (panel 1-3). Defects were detected at different depths, mostly in the periphery of the panel. When screening the specimen from the boundary to the center, defects were detected closer to the middle plane of the

Table 4
Summary of experiments.

Geometry	Labels		$I_0/\overline{M}$ (m s^{-1})	Normalized peak deflection δ_{max}/L	Deflection rate[b]	Deflection profile shape	Failure[c]	Damage[d]
Solid panel	**1-1**		116	0.151	1	Parabolic	–	M−
	1-2		166	0.188	2	Parabolic	–	M−
	1-3		227	0.257	3	Conical	–	M+, D+ center
	1-4		314	0.350	5	Conical	Total (cracks)	M+, D+, F+ total
	1-5		416	–	5	Conical	Total (cracks)	M+, D+, F+ total
Symmetrical sandwich	**2-1**	WS[a]	217	0.198	1	Parabolic	–	M−
		AS[a]					–	D−
	2-2	WS	351	0.222	1	Parabolic	cracks (boundary)	M−, F-,
		AS					–	D−
	2-3	WS	495	0.268	2	Parabolic	cracks (center and boundary)	M−,D+,F+
		AS					–	D−
	2-4	482	0.213	1	Parabolic	–	–	
Asymmetrical sandwich	**3-1**	WS	350	0.222	1	Parabolic	cracks (boundary)	M−,F−
		AS					–	D−
	3-2	WS	592	0.291	3	Parabolic	total	M+,D+,F+
		AS					shearing (boundary)	M+,D+,F−

[a] WS and AS stand for the panel "airside" and "waterside", respectively.
[b] The deflection rate is represented by a qualitative number varying between 1 and 5 (from the lowest to the highest rate).
[c] Absence of failure corresponds to a minus sign.
[d] Each damage mechanism is labeled with a letter: M stands for matrix damage, D for delamination and F for fiber damage. Damage intensity is described with plus and minus signs.

panel. In sandwich panels, the most significant feature detected by NDE was a delamination ring ($\sim$10 mm wide) on the airside of the panel. Delamination on the waterside facesheet was confined to the center region where the fluid–structure interaction effect is dominant. The technique did not provide precise information on through thickness position and total number of delaminated interfaces. Such information was later obtained by optical microscopy performed on selected cross-sections together with a quantitative estimation of matrix damage for different applied impulses. Matrix damage was estimated from measured crack densities by applying a variational formulation introduced by Hashin (1985).

The quantified matrix damage was maximal in the center of solid panels, where biaxial stretching is the highest, and decreases towards the boundary of the panel. At low impulse (experiment 1-1, $I_0/\overline{M}=116$ m s^{-1}) the damage distribution was spread through the thickness. At higher impulses damage was higher on the airside where higher superposition of bending and stretching occurred. At sufficiently high impulses (e.g., experiment 1-3, $I_0/\overline{M}=227$ m s^{-1}), more uniform through thickness damage was identified with values in some fabrics reaching $d=1$ at the center and near the panel edge. This saturation is likely associated with an exhaustion of dissipated energy by matrix damage. This is consistent with the pronounced fiber failure observed at high impulses (experiments 1-4 and 1-5, $I_0/\overline{M}>310$ m s^{-1}).

The experimental data here reported should be highly useful to those interested in developing models capable to predict the dynamic behavior and damage evolution of fiber composite laminated panels of solid and sandwich construction. Models for the experiments here reported are currently being developed (Latourte et al., 2009; Espinosa et al., 2009) and employed to assess their predictive capabilities. A detailed description of the model calibration procedure, comparison to experimental results and assessment of their predictive capabilities will be presented in a companion paper.

Acknowledgments

This research was carried out under the financial support of the Office of Naval Research (ONR) under grant number N00014-08-1–1055. The support and encouragement provided by Dr. Rajapakse through the study is greatly appreciated. D. Grégoire is grateful to the French Ministry of Defense (DGA/D4S) for its support through Grant no. 0860021 to visit Northwestern University as a research associate. We acknowledge Alex Ray at Sonoscan Inc. for conducting the pulse-echo C-scan measurements. Special thanks go to Arnaud Blouin for the assistance provided to set up and conduct the Fluid–Structure Interaction experiments during his Northwestern internship.

Appendix A. Deflection profile histories in solid and sandwich panels

A.1. Deformation histories in solid panels

A set of shadow Moiré images recorded during experiment 1-2 is shown in Fig. 21. Using the fringe processing technique introduced in Espinosa et al. (2006), deflection profiles associated with each image were obtained. The same procedure was used in all experiments. Figs. 22 and 23 present, respectively, the deflection profile histories (increasing and spring back phases) obtained by the shadow Moiré method for experiments 1-1 and 1-3 (impulses per areal mass $I_0/\overline{M}$ of 116 and 227 m s^{-1}, respectively). Deflection profiles were computed for each experiment but here we plot only the complete profile evolutions related to experiments 1-1 and 1-3 to highlight different features associated with variations in impulse level. Both deflection δ and dimensionless deflection δ/L versus the normalized radial position r/L are plotted.

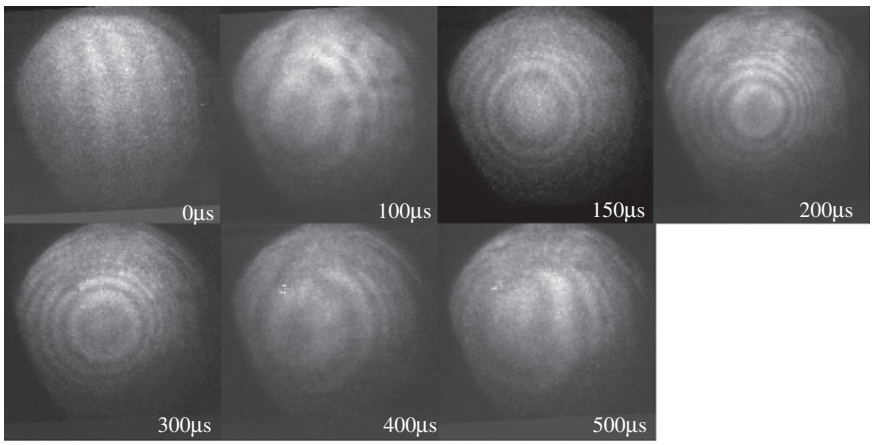

Fig. 21. Example of high speed camera pictures acquired during the dynamic event. Images shown here correspond to the monolithic panel tested at $I_0/\overline{M}=166$ m s^{-1}. Time $t=0$ is set when the pressure wave reaches the specimen.

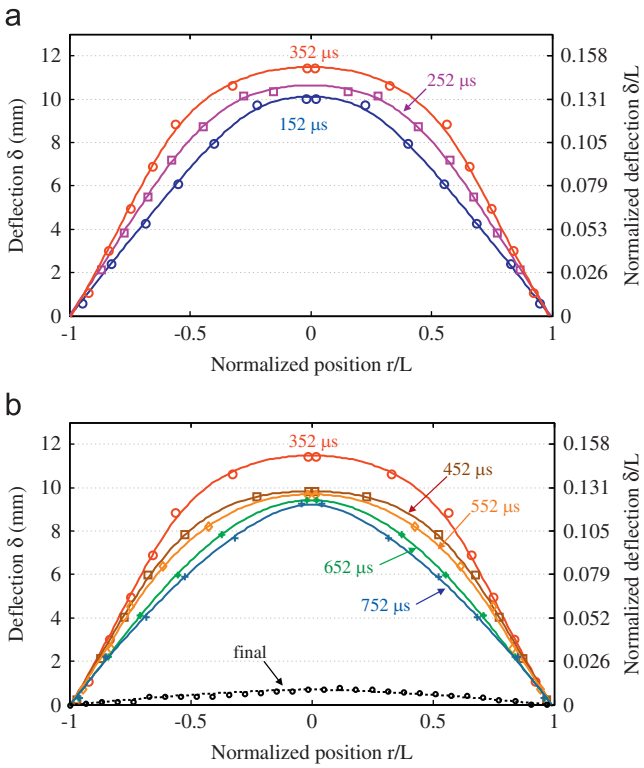

Fig. 22. Deflection profile history for experiment 1-1 tested at $I_0/\overline{M}=116\ \mathrm{m\,s^{-1}}$: (a) increasing deformation phase and (b) spring back deformation phase, including final profile measured post-mortem.

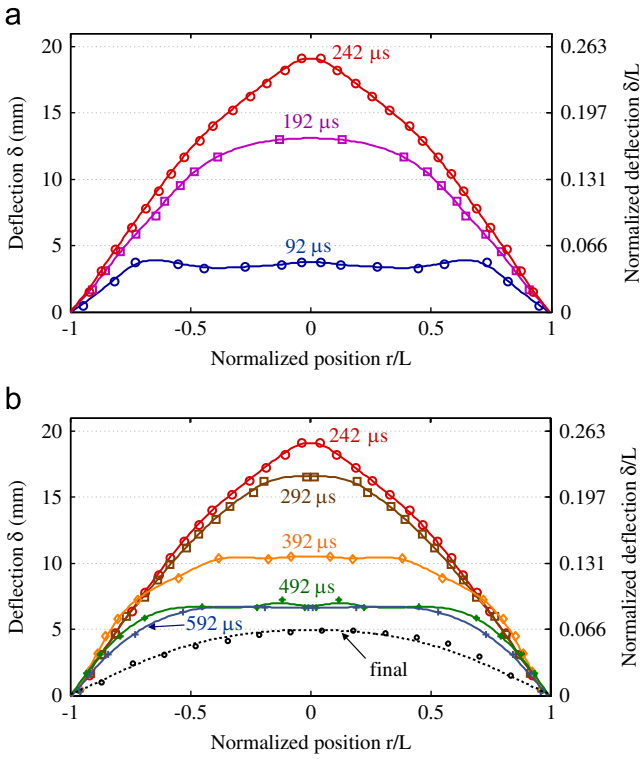

Fig. 23. Deflection profile history for experiment 1-3 tested at $I_0/\overline{M}=227\ \mathrm{m\,s^{-1}}$: (a) increasing deformation phase and (b) spring back deformation phase, including final profile measured post-mortem.

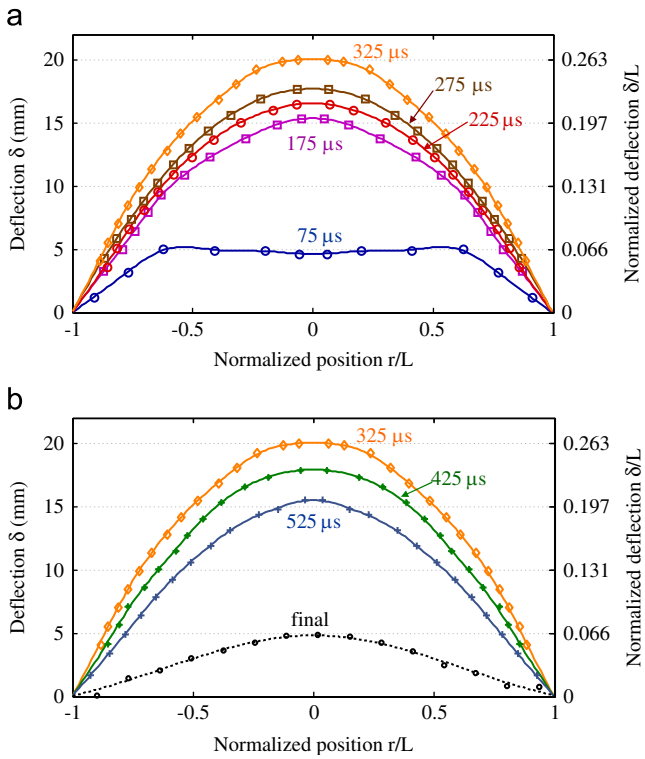

Fig. 24. Deflection profile histories corresponding to experiment 2-3 tested at $I_0/\overline{M}=495\ \mathrm{m\,s^{-1}}$: (a) increasing deformation phase and (b) spring back deformation phase, including final profile measured post-mortem.

Parameters are normalized by the composite panel radius $L=76.2$ mm. The increasing and spring back phases of the deformation are separately plotted for the sake of clarity.

It is interesting to note that in experiment 1-1 (Fig. 22), the deformed shape is more parabolic, which is an indication of more bending-type deformation. By contrast, in experiment 1-3 (Fig. 23) after 192 µs the panel deformed shape is more conical consistent with a membrane dominated deformation regime.

A.2. Deformation histories in sandwich panels

Fig. 24 shows deflection profile histories (increasing and spring back phases) obtained by the shadow Moiré method for a symmetrical sandwich panel, experiment 2-3 with impulse per areal mass of $495\ \mathrm{m\,s^{-1}}$. Both deflection δ and normalized deflection δ/L versus dimensionless radial position r/L are plotted. The radial position is normalized by the composite panel radius $L=76.2$ mm. Similar deflection profile histories were obtained for all the tested sandwich panels.

Appendix B. Non-destructive evaluation technique and damage maps

In the NDE technique introduced in Section 3.2, for each pixel, a pulse is emitted by a 10 MHz transducer. The generated wave propagates through the scanned material and detects changes in acoustic impedance. For example, a large planar void (delamination) will reflect the entire wave. The reflected signal is captured by the same transducer used for emission. The scanning sequence used in solid and sandwich panels is illustrated in Fig. 25a and b, respectively. Scanning from both waterside and airside of the FSI experimental setup were performed.

An example of two signals I_s recorded by the transducer at different locations is shown in Fig. 26a. The first noticeable spike corresponds to the interface between the water medium and the sample. Several spikes follow, of decaying amplitude. The captured signals are decomposed into time domains referred to as gates 1–6 and labeled $\{s_i,\ i=1,\ldots,6\}$. Within each gate, the pixel value I_R is taken as the absolute value of the signal peak amplified by a gain factor calibrated such that an intensity I_R of 1 corresponds to a total reflection of the signal. Such conditions are obtained when a large void (low impedance medium) is encountered within the gate. On the other hand, an intensity I_R of 0 corresponds to the absence of signal reflection. This will occur when the scanned medium is uniform within the gate (no change in impedance), but also if a defect above the current gate already reflected the signal (shadowing effect). As a consequence, the pulse-echo technique will detect the outer envelope of defects in the composite panel. In other words, when delamination occurs at multiple interfaces, only the outermost delamination patches will be seen by the pulse-echo technique.

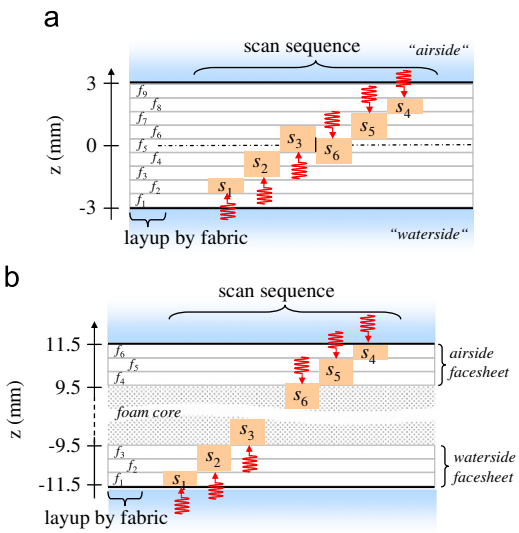

Fig. 25. Representation of the gate sequence s_i for C-scans performed by pulse-echo technique on monolithic (a) and symmetrical sandwich (b) panels. The characteristic times related to the gates s_i are detailed in Table 5. For illustrative purpose, the fabrics f_i are shown on the graphs.

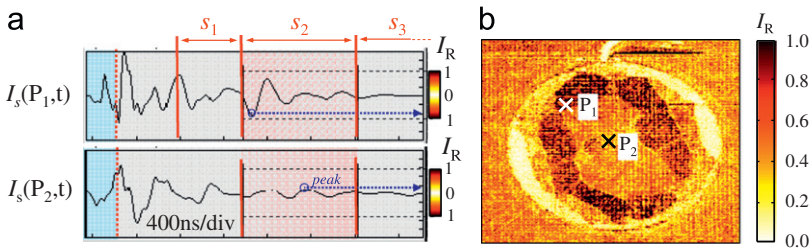

Fig. 26. (a) Reflected signals I_s obtained at two different pixels positions P_1 and P_2 for solid panel 1-2. The panel/water interface corresponds to the red dashed line, and the solid red lines define the gate bounds. (b) C-scan for gate s_2 and location of pixel positions P_1 and P_2. (For interpretation of the references to color in this figure legend, the reader is referred to the web version of this article.)

Table 5
Gates selected to generate the C-scan maps from the pulse-echo scans. Times t_i and t_f correspond to the beginning and the end of each record.

Gate#	t_i (μs)	t_f (μs)	Solid panels		Sandwich panels	
			$z_i^{(1)}$ (mm)	$z_f^{(1)}$ (mm)	$z^{i(2)}$ (mm)	$z_f^{(2)}$ (mm)
s_1	0.827	1.392	−2.25	−1.5	−11.5	−10.75
s_2	1.392	2.468	−1.5	−0.25	−10.75	−9.5
s_3	2.468	3.512	−0.25	1	−9.5	−8.25
s_4	0.827	1.392	−1	0.25	8.25	9.5
s_5	1.392	2.468	0.25	1.5	9.5	10.75
s_6	2.468	3.512	1.5	2.25	10.75	11.5

Each specimen was imaged separately from both its waterside and airside. For each scan, the reflected signal captured by the transducer at each position was processed to generate three distinct images corresponding to different gate times summarized in Table 5. These times were then translated into height z assuming a group wave velocity of 2390 m/s calculated from the GRP density and transverse modulus. This assumption is valid here since the wave number is high enough to prevent dispersive effects (Nayfeh and Anderson, 2000).

From the different gate times and the group velocity, one can obtain relative scan depths. The panel surface position was first identified from the signal to obtain the absolute scan depth z given in the coordinate system of the panel. In the case of monolithic panels, the surface was located using the signal I_s plotted in Fig. 26, and assuming that the first spikes correspond to the specimen surface. In the case of sandwich panels, the position of the surface was calculated by correlating the measured I_R maps and the microscopy analysis presented in Section 3.3.

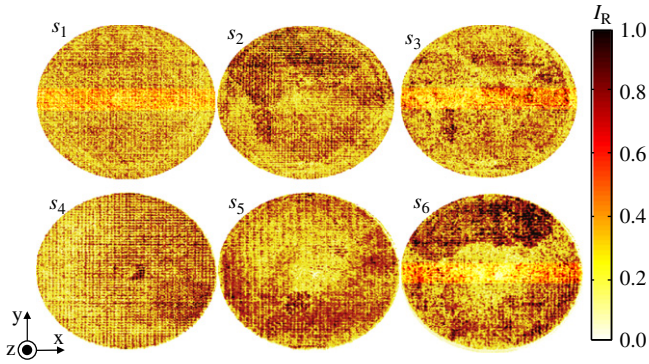

Fig. 27. C-scans obtained for experiment 1-1 at the impulse per areal mass of $I_0/\overline{M}=116$ m s^{-1}, waterside (gates s_1–s_3) and airside (gates s_4–s_6).

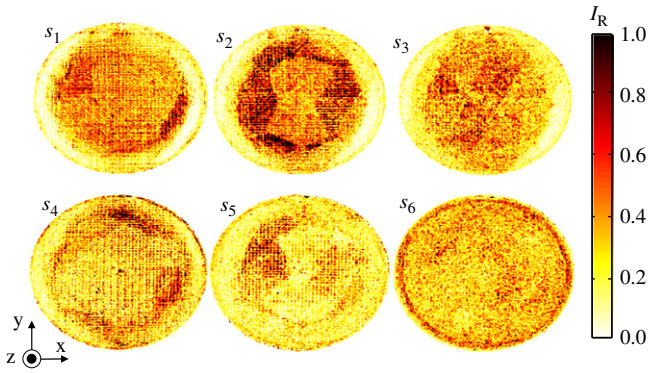

Fig. 28. C-scans obtained for solid panel tested at the impulse per areal mass of $I_0/\overline{M}=227$ m s^{-1}, exp. 1–3, waterside (gates s_1–s_3) and airside (gates s_4–s_6).

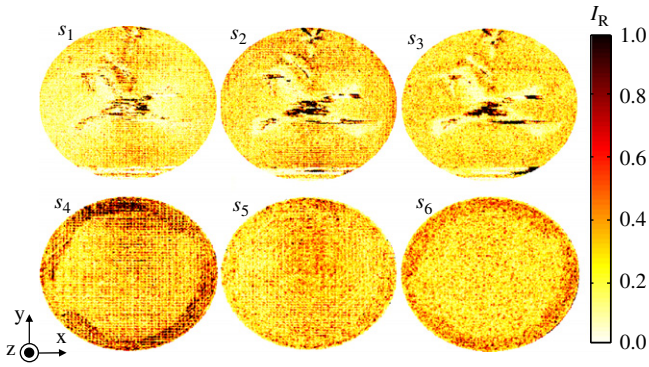

Fig. 29. C-scans obtained for sandwich panel 2-3 tested at the impulse per areal mass of $I_0/\overline{M}=495$ m s^{-1}, waterside (gates s_1–s_3) and airside (gates s_4–s_6).

The scans corresponding to the monolithic panel 1-1 tested at low impulse ($I_0/\overline{M}=116$ m s^{-1}) are shown in Fig. 27. The maps have been cropped to conform to the circular section of the panel subjected to water pressure during the FSI experiment. All images show a textured pattern consistent with the fabric weave of the composite. No significant feature except the texture can be noticed for the outermost gates s_1 and s_4, and most of the features are seen in gates s_2 and s_6. As illustrated in Fig. 25, there is an overlap between these two gates, which could explain the similitude in the observed I_R patterns. Although the behavior of the material is expected to be isotropic (the layup is quasi-isotropic) and the applied impulse is symmetric, the I_R patterns (associated to delamination) are asymmetrical and are more pronounced in the top region of the panel.

The scans corresponding to the monolithic panel tested at higher impulse ($I_0/\overline{M}=227$ m s^{-1}, exp. 1-3) are shown in Fig. 28. I_R maps corresponding to the outermost gates s_1 and s_4 show a bright ring in the periphery. These low values of I_R

correspond to the shadowing effect discussed earlier in this section. They indicate the presence of delamination patches above the imaged region of the panel (the gates do not cover the entire thickness as seen in Fig. 25). On all the scans except for s_4, where the signal-to-noise ratio seems to be poor, darker patterns are noticeable inside the white rings previously discussed, and correspond to delamination patches within the map gates. A central portion of the maps, with an hourglass shape, does not show strong reflection features. The feature is more evident on maps s_2 and s_5. Reflection features in this central region seem to be present in map s_3, which encompass the mid-plane of the panel. As discussed in Section 3.3, these features are consistent with delamination patterns observed in through thickness cross-sections.

The scans corresponding to the symmetric sandwich panel tested at the impulse $I_0/\overline{M}=495$ m s^{-1} (exp. 2-3) are shown in Fig. 29. The scans corresponding to the waterside exhibit a cross-shaped pattern. This feature is correlated to fiber fracture (see Fig. 14). Another radial crack, at the top of s_1–s_3, is adjacent to the boundary and corresponds to a macroscopic fracture observable in Fig. 14a and b. A dark narrow ring is clearly visible on maps s_4 and s_6 and less visible on map s_5. It corresponds to delamination patches within the mapped gates.

References

Abrate, S., 1991. Matrix cracking in laminated composites: a review. Composites Engineering 1 (6), 337–353.

Bhuiyan, M.A., Hosur, M.V., Jeelani, S., 2009. Low-velocity impact response of sandwich composites with nanophased foam core and biaxial (+/− 45 degrees) braided face sheets. Composites Part B—Engineering 40 (6), 561–571.

Daniel, I.M., Ishai, O., Daniel, I., 2006. Engineering Mechanics of Composite Materials. Oxford University Press, New York.

Dear, J.P., Arora, H., Hooper, P., 2009. Blast resistance of sandwich composite structures. In: ONR Review Meeting Solid Mechanics—Marine Composites and Sandwich Structures. University of Maryland.

Deshpande, V.S., Fleck, N.A., 2005. One-dimensional response of sandwich plates to underwater shock loading. Journal of the Mechanics and Physics of Solids 53 (11), 2347–2383.

Dharmasena, K., Queheillalt, D., Wadley, H., Dudt, P., Chen, Y., Knight, D., Evans, A., Deshpande, V., 2010. Dynamic compression of metallic sandwich structures during planar impulsive loading in water. European Journal of Mechanics-A/Solids 29, 56–67.

Espinosa, H., Lee, S., Moldovan, N., 2006. A novel fluid structure interaction experiment to investigate deformation of structural elements subjected to impulsive loading. Experimental Mechanics 46 (6), 805–824.

Espinosa, H.D., Dwivedi, S., Lu, H.C., 2000. Modeling impact induced delamination of woven fiber reinforced composites with contact/cohesive laws. Computer Methods in Applied Mechanics and Engineering 183 (3–4), 259–290.

Espinosa, H.D., Gregoire, D., Latourte, F., Ramaswamy, R.B. Failure modes in solid and sandwich composite panels subjected to underwater impulsive loads. In: ICSS9 2009, Pasadena, California, USA.

Forghani, A., Vaziri, R., 2009. Computational modeling of damage development in composite laminates subjected to transverse dynamic loading. Journal of Applied Mechanics—Transactions of the ASME 76, 5.

Grogan, J., Tekalur, S.A., Shukla, A., Bogdanovich, A., Coffelt, R.A., 2007. Ballistic resistance of 2d and 3d woven sandwich composites. Journal of Sandwich Structures & Materials 9 (3), 283–302.

Hall, D.J., 1989. Examination of the effects of underwater blasts on sandwich composite structures. Composite Structures 11 (2), 101–120.

Hashin, Z., 1980. Failure criteria for unidirectional fiber composites. Journal of Applied Mechanics—Transactions of the ASME 47 (2), 329–334.

Hashin, Z., 1985. Analysis of cracked laminates: a variational approach. Mechanics of Materials 4 (2), 121–136.

Hashin, Z., 1986. Analysis of stiffness reduction of cracked cross-ply laminates. Engineering Fracture Mechanics 25 (5–6), 771–778.

Hashin, Z., Rotem, A., 1973. Fatigue failure criterion for fiber reinforced materials. Journal of Composite Materials 7 (Oct.), 448–464.

Hinton, M.J., Kaddour, A.S., Soden, P.D., 2002. A comparison of the predictive capabilities of current failure theories for composite laminates, judged against experimental evidence. Composites Science and Technology 62 (12–13), 1725–1797.

Hoo Fatt, M.S., Palla, L., 2009. Analytical modeling of composite sandwich panels under blast loads. Journal of Sandwich Structures and Materials 11, 357.

Hosur, M.V., Mohammed, A.A., Zainuddin, S., Jeelam, S., 2008. Processing of nanoclay filled sandwich composites and their response to low-velocity impact loading. Composite Structures 82 (1), 101–116.

Hutchinson, J.W., Xue, Z.Y., 2005. Metal sandwich plates optimized for pressure impulses. International Journal of Mechanical Sciences 47, 545–569.

Johnson, H.E., Louca, L.A., Mouring, S., Fallah, A.S., 2009. Modelling impact damage in marine composite panels. International Journal of Impact Engineering 36 (1), 25–39.

Jones, N., 1989. Structural Impact. Cambridge University Press.

Ladeveze, P., Lubineau, G., 2002. An enhanced mesomodel for laminates based on micromechanics. Composites Science and Technology 62 (4), 533–541.

Ladeveze, P., Lubineau, G., Violeau, D., 2006. A computational damage micromodel of laminated composites. International Journal of Fracture 137 (1–4), 139–150.

Latourte, F., Gregoire, D., Ramaswamy, R.B., Espinosa, H.D. Performance of composite panels subjected to impulsive loadings. In ICCM17 2009, Edinburgh.

LeBlanc, J., Shukla, A., 2010. Dynamic response and damage evolution in composite materials subjected to underwater explosive loading: an experimental and computational study. Composite Structures 92 (10), 2421–2430.

Liang, Y., Spuskanyuk, A.V., Flores, S.E., Hayhurst, D.R., Hutchinson, J.W., McMeeking, R.M., Evans, A.G., 2007. The response of metallic sandwich panels to water blast. Journal of Applied Mechanics 74 (1), 81–99.

Lim, S.G., Hong, C.S., 1989. Effect of transverse cracks on the thermomechanical properties of cross-ply laminated composites. Composites Science and Technology 34 (2), 145–162.

Marshall, D.B., Cox, B.N., Evans, A.G., 1985. The mechanics of matrix cracking in brittle-matrix fiber composites. Acta Metallurgica 33 (11), 2013–2021.

Mori, L.F., Lee, S., Xue, Z.Y., Vaziri, A., Queheillalt, D.T., Dharmasena, K.P., Wadley, H.N.G., Hutchinson, J.W., Espinosa, H.D., 2007. Deformation and fracture modes of sandwich structures subjected to underwater impulsive loads. Journal of Mechanics of Materials and Structures 2 (10), 1981–2006.

Mori, L.F., Queheillalt, D.T., Wadley, H.N.G., Espinosa, H.D., 2009. Deformation and failure modes of i-core sandwich structures subjected to underwater impulsive loads. Experimental Mechanics 49 (2), 257–275.

Mouritz, A.P., Townsend, C., Khan, M.Z.S., 2000. Non-destructive detection of fatigue damage in thick composites by pulse-echo ultrasonics. Composites Science and Technology 60 (1), 23–32.

Mouritz, A.P., Gellert, E., Burchill, P., Challis, K., 2001. Review of advanced composite structures for naval ships and submarines. Composite Structures 53 (1), 21–42.

Nayfeh, A.H., Anderson, A.M.J., 2000. Wave propagation in layered anisotropic media with applications to composites. The Journal of the Acoustical Society of America 108 (2), 471–472.

Nurick, G.N., Martin, J.B., 1989. Deformation of thin plates subjected to impulsive loading. A review, part ii: experimental studies. International Journal of Impact Engineering 8 (2), 171–186.

Nurick, G.N., Shave, G.C., 1996. The deformation and tearing of thin square plates subjected to impulsive loads—an experimental study. International Journal of Impact Engineering 18 (1), 99–116.

Porfiri, M., Gupta N., 2009. A review of research on impulsive loading of marine composites. In: Major Accomplishments in Composite Materials and Sandwich Structures. pp. 169–194.
Puck, A., Schurmann, H., 1998. Failure analysis of frp laminates by means of physically based phenomenological models. Composites Science and Technology 58 (7), 1045–1067.
Rajendran, R., Narashimhan, K., 2001. Performance evaluation of hsla steel subjected to underwater explosion. Journal of Materials Engineering and Performance 10 (1), 66–74.
Rajendran, R., Narasimhan, K., 2006. Deformation and fracture behaviour of plate specimens subjected to underwater explosion—a review. International Journal of Impact Engineering 32 (12), 1945–1963.
Schubel, P.M., Luo, J.J., Daniel, I.M., 2005. Low velocity impact behavior of composite sandwich panels. Composites Part A—Applied Science and Manufacturing 36 (10), 1389–1396.
Singh, C.V., Talreja, R., 2009. A synergistic damage mechanics approach for composite laminates with matrix cracks in multiple orientations. Mechanics of Materials 41 (8), 954–968.
Soden, P.D., Hinton, M.J., Kaddour, A.S., 1998. A comparison of the predictive capabilities of current failure theories for composite laminates. Composites Science and Technology 58 (7), 1225–1254.
Soden, P.D., Hinton, M.J., Kaddour, A.S., 2002. Biaxial test results for strength and deformation of a range of e-glass and carbon fibre reinforced composite laminates: failure exercise benchmark data. Composites Science and Technology 62 (12–13), 1489–1514.
Soden, P.D., Kaddour, A.S., Hinton, M.J., 2004. Recommendations for designers and researchers resulting from the world-wide failure exercise. Composites Science and Technology 64 (3–4), 589–604.
Tagarielli, V.L., Deshpande, V.S., Fleck, N.A., 2007. The dynamic response of composite sandwich beams to transverse impact. International Journal of Solids and Structures 44 (7–8), 2442–2457.
Teeling-Smith, R.G., Nurick, G.N., 1991G. The deformation and tearing of thin circular plates subjected to impulsive loads. International Journal of Impact Engineering 11 (1), 77–91.
Tekalur, S.A., Shivakumar, K., Shukla, A., 2008J. Mechanical behavior and damage evolution in e-glass vinyl ester and carbon composites subjected to static and blast loads. Composites Part B—Engineering 39 (1), 57–65.
Tilbrook, M., Deshpande, V., Fleck, N., 2009. Underwater blast loading of sandwich beams: regimes of behaviour. International Journal of Solids and Structures 46, 3209–3221.
Vaziri, A., Xue, Z.Y., Hutchinson, J.W., 2007. Performance and failure of metal sandwich plates subject to shock loading. Journal of Mechanics of Materials and Structures.
Xue, Z., Hutchinson, J.W., 2004. A comparative study of impulse-resistant metal sandwich plates. International Journal of Impact Engineering 30 (10), 1283–1305.
Xue, Z.Y., Hutchinson, J.W., 2003. Preliminary assessment of sandwich plates subject to blast loads. International Journal of Mechanical Sciences 45 (4), 687–705.
Zenkert, D., Shipsha, A., Bull, P., Hayman, B., 2005. Damage tolerance assessment of composite sandwich panels with localised damage. Composites Science and Technology 65 (15–16), 2597–2611.